

Phase field model for irradiation-induced crack propagation in outer coating layers of TRISO particle fuel in space reactor applications

Lin Peng^{1,2}; Simiao Tang^{1,2*}; Songyang Li^{1,2}; Longxiang Zhu^{1,2}; Qiang Lian^{1,2}; Luteng Zhang^{1,2}; Liangming Pan^{1,2}

1. Key Laboratory of Low-grade Energy Utilization Technologies and Systems, Ministry of Education, Chongqing University, Chongqing 400044, China;
2. Department of Nuclear Engineering and Technology, Chongqing University, Chongqing 400044, China.

* Corresponding author: Email address: simiao_tang@cqu.edu.cn

Abstract

As an advanced fuel form, TRISO particle fuel is relatively reliable due to the excellent capability of its thin coating layers to contain fission products, but it is still prone to cracks or pores in the coatings during production, transportation, and usage. These irregular geometries can significantly impact their ability to maintain structural integrity. Therefore, in order to advance the use of TRISO particles in space reactors, analyzing and predicting the crack propagation in their coatings is crucial. This model introduces the material properties of TRISO particles, irradiation behavior, and fission gas release model, and establishes a phase field model to investigate the crack propagation characteristics of the outer three coatings of TRISO particles. The accuracy of this model for TRISO particle performance was verified through an IAEA benchmark problem and a comparison with BISON program results for TRISO particles. The reliability of the phase field model for crack simulation was validated by analyzing a notched tensile plate and Kalthoff experiment. The effects of a crack in the IPyC layer, a residual pore in the SiC layer, a crack on the outer side of OPyC, and the simultaneous presence of a crack in the IPyC layer and a residual pore in the SiC layer, were studied in succession. The calculation results reveal that cracks in the IPyC layer cause debonding between the IPyC and SiC layers, but they are insufficient to propagate into the SiC layer during the early stages of burnup. Residual pores in the SiC layer lead to the complete fracture of the coating layers, primarily due to excessive gas pressure from the inner IPyC layer rather than the weakening effect of the pores on the structure. Cracks in the OPyC layer cause concentrated tensile stress on the outer side of the SiC layer during the early stages of burnup, which alters the crack propagation path in the coating layers during the later stages of burnup. Therefore, in addition to using material detection techniques to screen out TRISO particles with excessive defects before the production of FCM pellets, it is essential to enhance the ability of coating layers to maintain structural integrity and implement fundamental measures such as expelling accumulated gases from the particles. These actions are crucial for the safe and stable operation of TRISO particle fuel in space reactors.

Key words: TRISO particle, Phase field, Fracture mechanics, Nuclear engineering, Space reactor

1. Introduction

Based on the stringent requirements for reactor stability and safety, several Accident Tolerant Fuels (ATFs) have been developed and partially implemented [1-2], aiming to maintain fuel structural integrity and ensure reactor safety under both normal and even accident conditions. Among these, Fully Ceramic Microencapsulated (FCM) fuel stands out as a promising candidate [3]. It consists of TRistructural-ISotropic (TRISO) coated fuel particles dispersed within the Nano-Infiltration and Transient Eutectic-phase SiC (NITE-SiC) matrix. To ensure the stability of the entire fuel pellet, it is crucial to investigate its fundamental unit, the TRISO particle. A TRISO particle consists of a kernel surrounded by four consecutive coating layers, with its structure illustrated in Fig. 1. The kernel, which serves as the heat source for the reactor through nuclear reactions, can be made of UO_2 , UN, or UCO. The first coating layer, known as the Buffer layer, is composed of low-density pyrocarbon (PyC). It acts as a cushion, offering space for gaseous fission products while alleviating the stresses caused by kernel expansion on the outer coating layers [4]. The second coating layer is the Inner Pyrolytic Carbon (IPyC) layer, made of dense PyC. It prevents the internal structures from being corroded during manufacturing and keep the SiC layer shielded from damage caused by gaseous and solid fission products [5-6]. The next layer, the silicon carbide (SiC) layer, is deposited on the IPyC layer using the Chemical Vapor Deposition (CVD) method, referred to as CVD-SiC (to distinguish it from NITE-SiC). The SiC layer not only contains fission products but also serves as the main pressure shell to maintain the structural integrity of the TRISO particle [7-10]. Finally, the outermost layer is the Outer PyC (OPyC) layer, which acts as the last barrier for fission products and protects the CVD-SiC layer during the manufacturing process [5]. Owing to the multi-layered coating structure of TRISO particles, they can effectively contain fission products and maintain structural integrity, exhibiting excellent irradiation stability and thermo-mechanical performance [11-12].

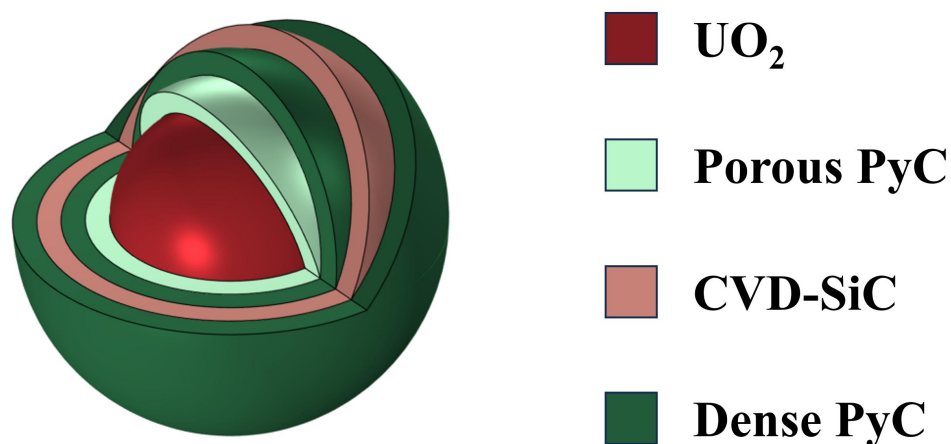


Fig. 1. Structure of a TRISO particle.

There has already been some basis established in the experimental and numerical studies of TRISO particles. Irradiation experiments have shown that, due to the porosity of the buffer layer, its volume undergoes shrinkage under neutron irradiation [13]. J. L. Hales et al. simulated TRISO particles using the BISON code [14], demonstrating the feasibility of numerical simulation for TRISO particles and validating the effectiveness of the program. C. Zhang et al. employed the COMSOL software to develop simulation methods for TRISO particles and FCM pellets [15–16], concluding that TRISO particles are relatively reliable under normal HTGR conditions. However, with the increasing demands of space exploration and deep-sea missions, the research and development of space reactors have become increasingly urgent [17–19]. In the previous study [20], the results had revealed that, mainly due to the requirements of space reactors for higher fuel temperatures, greater fission rates, and longer operational lifetimes, the internal gas pressure on the inner side of the IPyC layer significantly increases during the mid-to-late stages of burnup. This results in higher tensile stresses in SiC layer, greatly increasing its probability of failure. And cracks may even develop in the outer coating layers, potentially leading to the collapse of the TRISO particle, as showed in Fig. 2 [21]. The stability of nuclear fuels, cladding, and other structural components plays a critical role in reactor operation [22 and 23]. Therefore, studying the crack propagation characteristics of the outer coating layers in TRISO particles is of paramount importance. Only by exploring and predicting the mechanisms and influencing factors of crack initiation and propagation in the coating layers can the safe and stable application of TRISO particles and FCM fuel in space reactors be advanced.

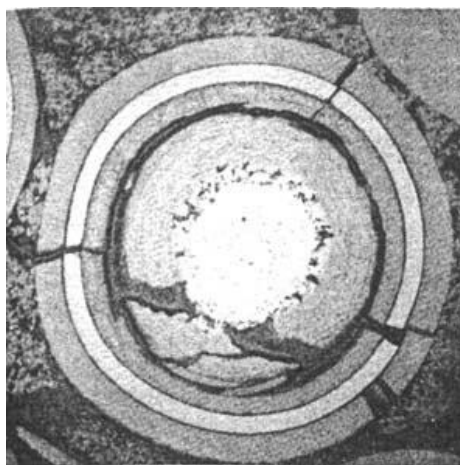


Fig. 2. Damage in TRISO particles from the P13T reactor [21].

In engineering problems where crack phenomena are difficult to investigate experimentally, researchers must rely on numerical simulation methods to predict complex crack paths [24], especially in scenarios like the intricate operating conditions of TRISO particles. Consequently, numerical simulation methods for crack propagation have seen some development in recent years. The discrete crack model introduces new boundaries for newly formed crack surfaces through adaptive mesh reconstruction [25]. The eXtended Finite Element Method (XFEM) enhances cracked elements by integrating discontinuous shape functions into the conventional Finite

Element Method (FEM) framework [26 and 27]. Similarly, the Cohesive Zone Model (CZM) simulates crack propagation by allowing displacement jumps along element boundaries, effectively modeling debonding and interfacial fractures, with cracks confined to predefined paths such as element edges [28-31]. And the phantom-node method models cracks independently of the mesh by overlapping elements at the crack location, allowing for discontinuous displacement without the need for enrichment functions [32]. Furthermore, element-erosion methods address fracture surfaces by setting the stresses of elements that meet the fracture criterion to zero, providing an alternative approach for simulating crack growth [33]. In summary, these complex crack simulation methods are challenging to apply to practical engineering problems. In contrast, the Phase-Field Method (PFM), which has gained significant attention in recent years, offers a more convenient approach for fracture simulation. It represents discrete cracks using a scalar field that smoothly transitions between intact and fully fractured material without treating cracks as physical discontinuities. This approach eliminates the need for explicit tracking of fracture surfaces, simplifying the simulation of crack propagation, branching, and merging in complex geometrical models. Moreover, by directly solving Partial Differential Equations (PDE) to determine the phase-field distribution, PFM adopts a numerical solution process similar to that of other physical fields, making crack simulation more convenient and accessible. Currently, several phase-field methods, including even multi-physics coupling approaches, have been developed based on software platforms such as ABAQUS [34], MOOSE [35], FEniCS [36], and COMSOL [37–39]. The phase field method has also been applied in the analysis of multiphysics coupled crack propagation [40-42], and has been used to analyze engineering problems such as hydraulic fracturing [43], cracking in concrete [44], coal seam fracturing [45], and hydrogen-induced cracking in pipelines [46]. However, studies on crack propagation in TRISO fuel particles remain limited. The microstructure of SiC in TRISO particles [47 and 48] and its oxidation behavior [49] have been experimentally studied, and the fracture strength of SiC has also been investigated [50]. A. M. Recuero, et al. employed an interaction integral approach to calculate stress intensity factors for cracks in the inner pyrolytic carbon layer perpendicular to the silicon carbide layer [51]. Y. Li simulated micro-defect-induced cracking in the IPyC layer of TRISO particles using the XFEM [52]. J. Tan et al. simulated cracks within the IPyC layer and at the interface between IPyC and SiC through phase field model, concluding that the combined effects of shrinkage and creep-induced stress relaxation play a crucial role in determining crack evolution and subsequently impact the stress distribution in the SiC layer [53]. Overall, the crack propagation characteristics in the coating layers of TRISO particles and their influencing factors still require further investigation.

This paper develops a phase-field model to simulate the crack propagation characteristics in the outer three coating layers of the TRISO particle. A 2D axisymmetric geometry model of the IPyC, CVD-SiC, and OPyC layers is constructed, incorporating material properties, irradiation behaviors, and fission gas pressure to simulate the operating conditions of the TRISO particle. The mechanical model was validated against the IAEA Coordinated Research Program (CRP-6) Case 8

benchmark, and the accuracy of the whole TRISO particle model was confirmed through comparison with BISON simulation results, which can be found in our previous study [20]. Subsequently, the crack propagation characteristics in the outer three layers are investigated. The influence of prefabricated crack depth in the IPyC layer on crack propagation and the maximum tensile stress in the SiC layer is first analyzed. Then, the effect of residual pores of different sizes in the SiC layer on crack initiation and propagation in the pressure vessel is studied. The impact of prefabricated cracks in the OPyC layer is also examined. Finally, the study explores the crack propagation characteristics caused by residual pores in the SiC layer following interface damage between the IPyC and SiC layers due to prefabricated cracks in the IPyC layer during the early burnup stage. Recommendations for limitations on crack and pore sizes and their impact on the stability of TRISO particles are also provided as part of the conclusions.

2. Model description

Fig. 3 illustrates the components of the model and their interactions, providing a basis for the subsequent explanation of the specific steps involved in model construction.

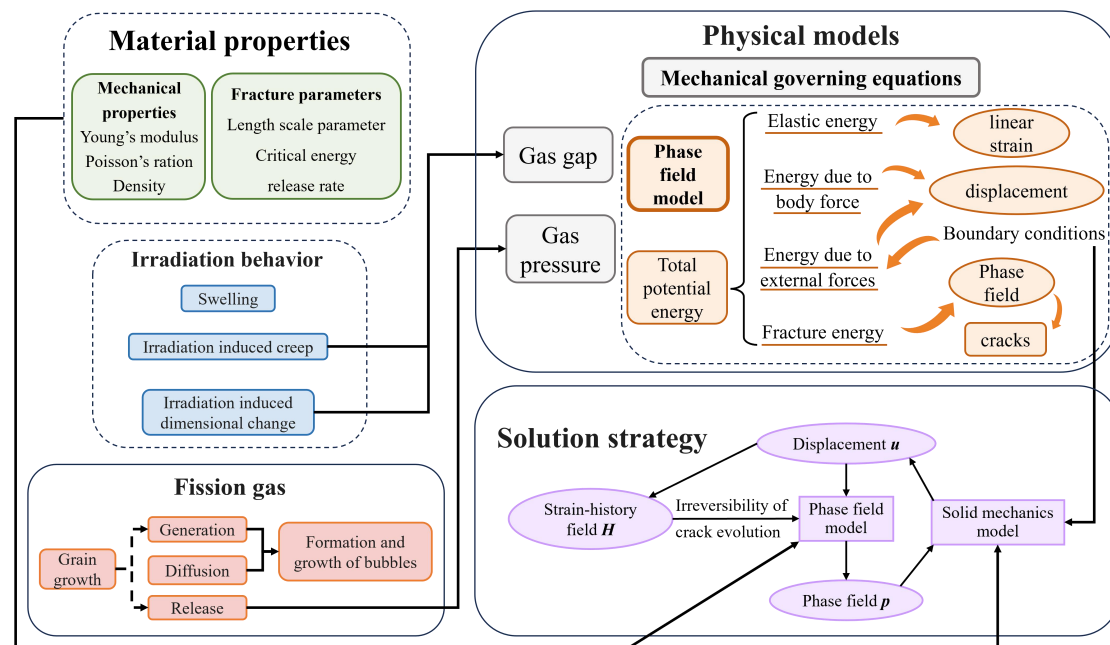


Fig. 3. Sketch map for components and their interactions involved in this study.

2.1 Mechanical governing equations and material properties

The mechanical calculation model, built with the "Solid Mechanics" module in COMSOL, is formulated based on Cauchy's equation, expressed as follows:

$$-\nabla \cdot \sigma = F_v \quad (1)$$

where σ is the Cauchy stress tensor, and F_v represents the body force per unit volume. The stress is calculated using a linear elastic constitutive model:

$$\sigma = [C][\varepsilon_e] \quad (2)$$

where C is the material matrix associated with Young's modulus and Poisson's ratio, and ε_e represents the elastic strain vector. The elastic strain is derived by subtracting the inelastic strain from the total strain, while the strain field is obtained from the displacement vector:

$$\varepsilon_e = \varepsilon - \varepsilon_{inel} \quad \varepsilon = \frac{1}{2} [\nabla \mathbf{u} + (\nabla \mathbf{u})^T] \quad (3)$$

$$\varepsilon_{inel} = \varepsilon_0 + \varepsilon_{ext} + \varepsilon_{cr} \quad (4)$$

where ε denotes the total strain, ε_{inel} is the inelastic strain, \mathbf{u} represents the displacement vector, and ε_0 , ε_{ext} and ε_{cr} correspond to the initial strain, external strain, and creep strain, respectively.

Experiments [13] and previous studies [20] have shown that during the early stages of burnup, the IPyC layer and the buffer layer separate, forming a gap that eliminates significant interaction and stress transfer between the two layers. Consequently, this study focuses on constructing the geometric model for the outer three coating layers only. Moreover, it has been shown in previous studies that the temperature within the outer three layers is nearly uniform [20], and therefore, a heat transfer model is not required. Additionally, due to the high mesh refinement requirements for crack simulation, a 2D axisymmetric model was developed to reduce computational costs, as shown in Fig. 4.

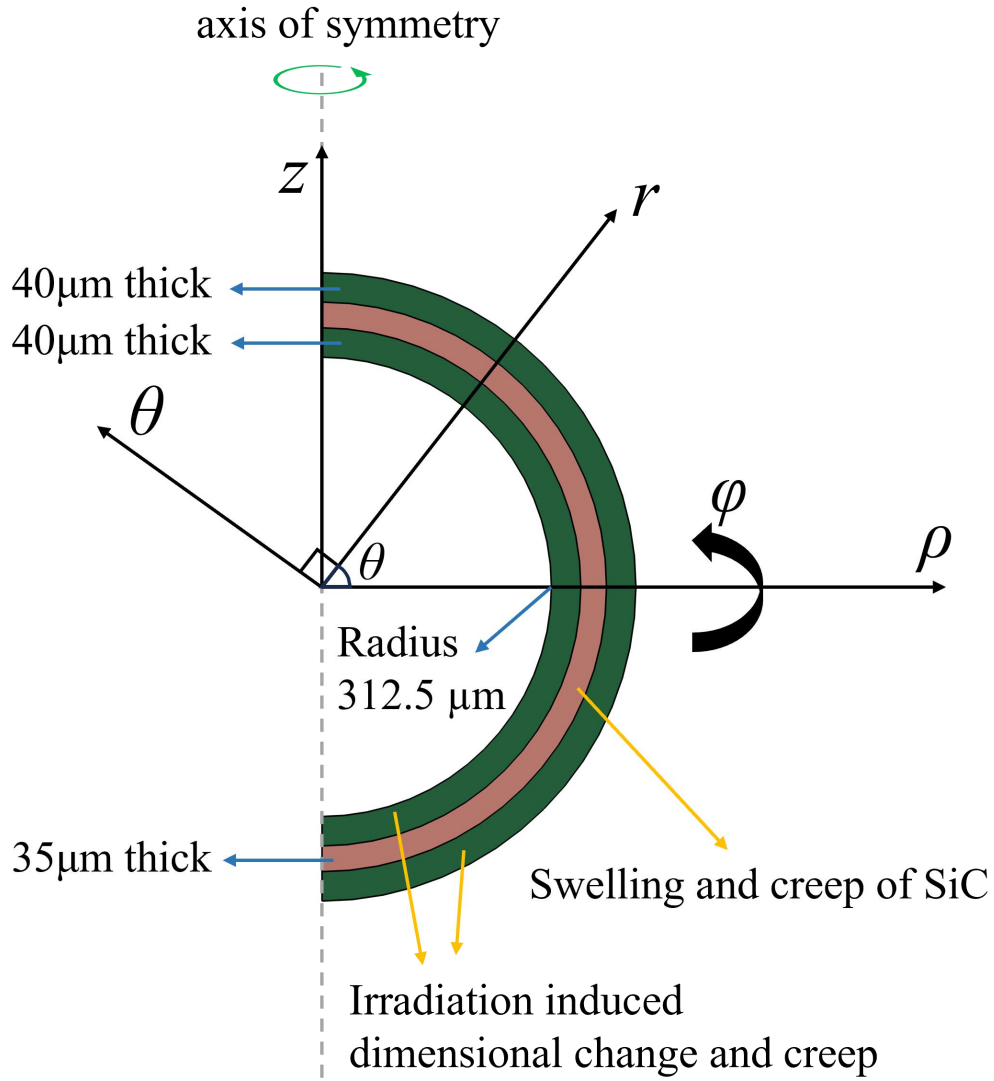


Fig. 4. 2D axisymmetric model of the TRISO particle and coordinate systems.

The relationship between the base vectors of the local spherical coordinates (r ; θ , φ) and those of the global cylindrical coordinates (ρ , z , φ) is given by:

$$\begin{cases} \mathbf{e}_r = \sin\left[\arctan\left(\frac{\rho}{z}\right)\right] \cdot \mathbf{e}_\rho + \cos\left[\arctan\left(\frac{\rho}{z}\right)\right] \cdot \mathbf{e}_z \\ \mathbf{e}_\theta = \cos\left[\arctan\left(\frac{\rho}{z}\right)\right] \cdot \mathbf{e}_\rho - \sin\left[\arctan\left(\frac{\rho}{z}\right)\right] \cdot \mathbf{e}_z \end{cases} \quad (5)$$

Regarding the mechanical properties of materials, the Young's modulus of PyC is expressed as following equations [54].

$$\begin{cases} E_r = E_0 (0.384 + 0.324\rho) (1.463 - 0.463BAF_0) (2.985 - 0.0662L_c) (1 + 0.23\phi) (1 + 0.00015(T - 20)) \\ E_\theta = E_0 (0.384 + 0.324\rho) (0.481 + 0.519BAF_0) (2.985 - 0.0662L_c) (1 + 0.23\phi) (1 + 0.00015(T - 20)) \end{cases} \quad (6)$$

where E_0 is 25.5 GPa, BAF_0 represents the initial degree of anisotropy, with a reasonable value of 1.03, L_c is the crystallite diameter size, with a value of 45 Å, and ρ , Φ , and T denote density (10^6 g/m³), neutron flux (10^{25} n/m²), and temperature (°C),

respectively.

The Poisson's ratio of IPyC is 0.21 [55], and its density is 1900 kg/m³ [14].

The Young's modulus of CVD-SiC is obtained experimentally [56]:

$$E = E_0 - B \cdot T \cdot e^{\left(\frac{T_0}{T}\right)} \quad (7)$$

where E_0 is 460 GPa, B is 0.04 GPa/K, and T_0 is 962 K.

The Poisson's ratio and density of SiC are set to 0.21 and 3210 kg/m³, respectively [56].

2.2 Irradiation behavior

Under the influence of neutron irradiation, PyC undergoes irradiation creep and irradiation-induced dimensional change, while SiC experiences creep and swelling. This section will explain the corresponding strain models.

2.2.1 Burnup

The burnup calculation in TRISO particles follows the burnup model proposed by Olander [57], where burnup is defined as the ratio of the number of fissions to the initial number of uranium atoms:

$$\beta = \frac{\dot{F}t}{N_f^0} \quad (8)$$

where \dot{F} and N_f^0 represent the fission rate per unit volume (fissions/m³/s) and the initial density of uranium atoms (atoms/m³) in the fuel, respectively. These quantities can be calculated using the following equations:

$$\dot{F} = q\sigma_f N_f \Phi \quad (9)$$

$$N_f^0 = \frac{D \cdot TD \cdot N_A}{M_{UO_2}} \quad (10)$$

In these equations, q is the enrichment (the ratio of fissile atoms to total uranium atoms), σ_f is the effective fission cross-section in the relevant neutron energy spectrum (barns), N_f is the total number of uranium atoms per unit volume, Φ is the neutron fluence (n/m²), D is the theoretical density ratio, TD is the theoretical density (g/cm³), N_A is Avogadro's constant, and M_{UO_2} is the molar mass of uranium dioxide (g/mol). There is a relationship between the burnup, Bu (defined by the energy released by the nuclide in MWd/kgU), and β (in %FIMA) given by the formula: $Bu = 9.5\beta$.

The fast neutron flux is calculated using the formula in BISON [58]:

$$\Phi = \int \dot{\Phi} dt \quad \dot{\Phi} = c \cdot P \quad (11)$$

where $\dot{\Phi}$ is the fast neutron flux, c is a conversion factor, typically 3×10^{13} (n/(m²·s)/(W/m)), and P is the linear heat rate (W/m).

2.2.2 Irradiation induced dimensional change, creep and swelling

During irradiation, both porous and dense PyC layers experience exposure to fast neutron fluence causing irradiation-induced dimensional changes. The irradiation strain rate for IPyC is different in the radial and tangential directions, as described by the following formulas from German [59]:

$$\dot{\epsilon}_r = -0.077e^{-\Phi} + 0.031 \quad (12)$$

$$\dot{\epsilon}_\theta = -0.036e^{-2.1\Phi} - 0.01 \quad (13)$$

where $\dot{\epsilon}$ and Φ denote the irradiation strain rate in units of 1/(10²⁵n/m²)/s and fast neutron fluence in 10²⁵n/m².

With prolonged neutron irradiation, the influence of radiation in the material's microstructure results in creep. The irradiation-induced creep rate of IPyC is described by [59]:

$$\dot{\epsilon}_{cr,r} = K[\sigma_1 - \nu_c(\sigma_2 + \sigma_3)]\dot{\Phi} \quad (14)$$

$$K = 2K_0[1 + 2.38(1.9 - \rho_0)] \quad (15)$$

$$K_0 = 1.996 \times 10^{-29} - 4.415 \times 10^{-32}T + 3.6544 \times 10^{-35}T^2 \quad (16)$$

where $\dot{\epsilon}_{cr,r}$ is creep rate in the radial direction in 1/s, the creep rates in other directions can be inferred in similar ways, K is the creep constant in m²/n /MPa, ρ_0 is initial density of porous or dense PyC in g/cm³, σ_i denote principal stresses in three directions, ν_c is Poisson ratio for creep, which is 0.5, and T is temperature in °C.

Silicon carbide is also subject to irradiation creep, which can be expressed by the following equation [59]:

$$\dot{\epsilon}_{cr} = K\dot{\Phi}\sigma_e \quad (17)$$

where the creep constant K is typically valued at 0.4×10^{-31} m²/n /MPa, $\dot{\Phi}$ and σ_e represent neutron flux in 10²⁵ n/m²/s and effective stress in MPa, respectively.

SiC also undergoes irradiation swelling, and the neutron-induced swelling between 1250°C and 1500°C is expressed by the following equation [59]:

$$\varepsilon_V = 0.0018 \left(1 - e^{-\frac{\phi}{\phi_0}} \right) + 1.297 \times 10^{-28} \phi \quad (18)$$

where ε_V is the volumetric strain caused by swelling, and ϕ_0 is 0.3396×10^{25} n/m².

At a neutron flux of 5×10^{17} n/m² and a temperature of 1500K, the irradiation-induced dimensional change (IIDC), swelling, and creep constants are shown in Fig. 5. As burnup progresses, PyC undergoes radial contraction followed by expansion, while the tangential direction continuously contracts. In contrast, the swelling and creep of SiC are relatively small compared to the irradiation behavior of PyC.

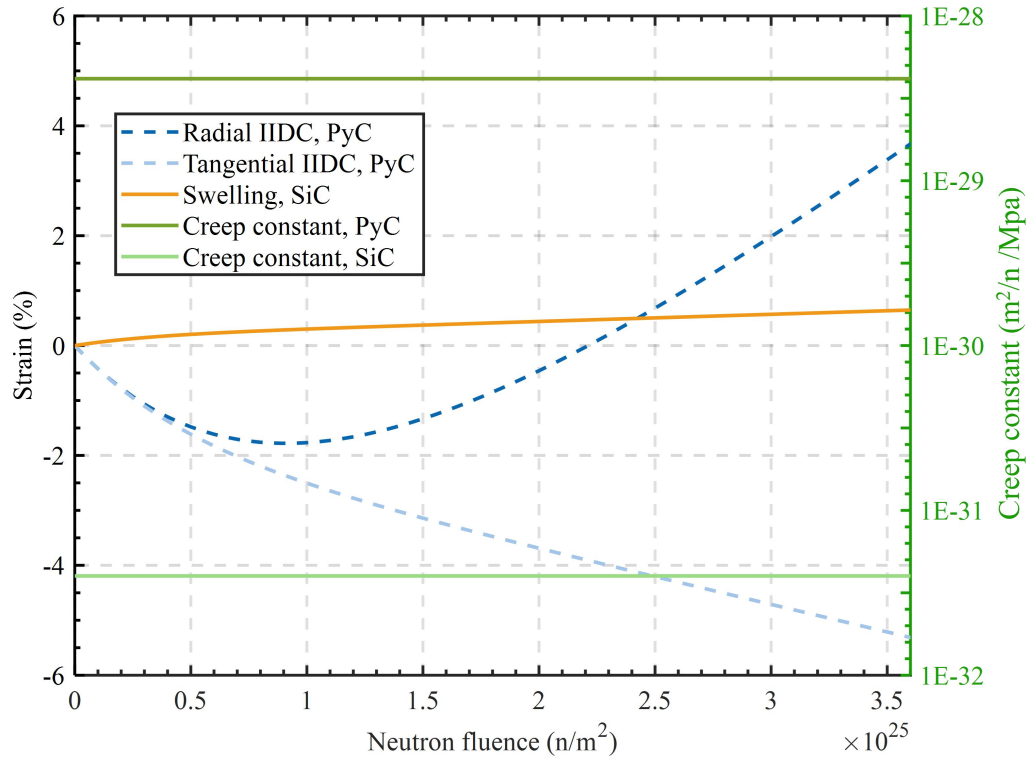


Fig. 5. Irradiation behavior of PyC and SiC.

2.2.3 Fission gas behavior

In actual nuclear fuels, fission gas atoms are generated within the grains of uranium dioxide due to nuclear fission reactions. These atoms can either form intragranular bubbles or diffuse to grain boundaries, where they may coalesce into intergranular bubbles. As the concentration of these gas atoms exceeds a critical threshold, influenced by temperature and other factors, they are released into the free volume, a process known as Fission Gas Release (FGR) [60-63]. After release, the fission gases interact with layers other than the kernel and generate internal pressure

on the IPyC layer. Therefore, accurately constructing the fission gas release model is critical, as the gas does not immediately release into free space and can affect the TRISO particle coatings dramatically. This significantly influences the accuracy of simulations related to TRISO particle fuel performance and failure assessments.

The fission gas model established in this study incorporates several key effects, including gas dissolution, atom diffusion, bubble growth, boundary concentration saturation, and the influence of grain growth and external pressure. These factors are modeled using equations and a series of conditions to account for gas atom coalescence and migration, as well as the resulting internal pressures on the inner side of IPyC. This model has been validated and further refined in previous studies [20]. The calculations in previous work are comprehensive and sufficient, so in this study, the gas pressure values calculated under the typical HTGR and more stringent space reactor conditions from previous research are directly used for the calculations, as shown in Fig. 6.

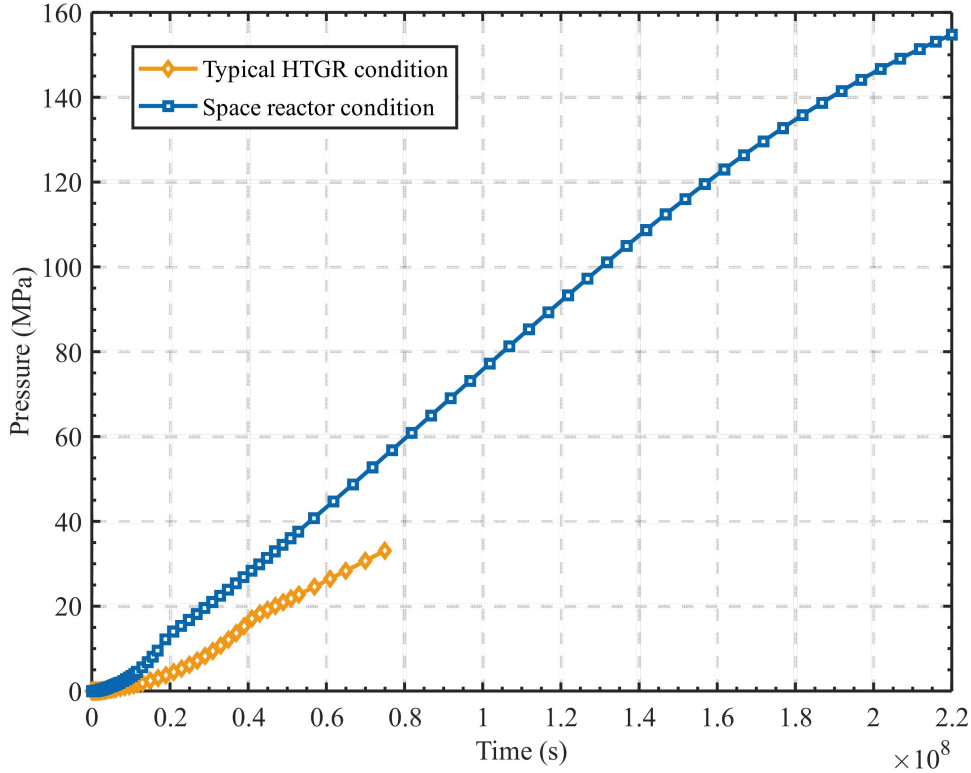


Fig. 6. Gas pressure on the inner surface of IPyC.

2.3 Phase field model for fracture

2.3.1 Brittle fracture theory

Consider a domain Ω with a pre-existing crack Γ , where Dirichlet boundary conditions and Neumann boundary conditions are applied at the boundaries. For instance, one side has fixed constraint, while the other side applies a given traction \mathbf{f} or displacement \mathbf{u} , as shown in Fig. 7.

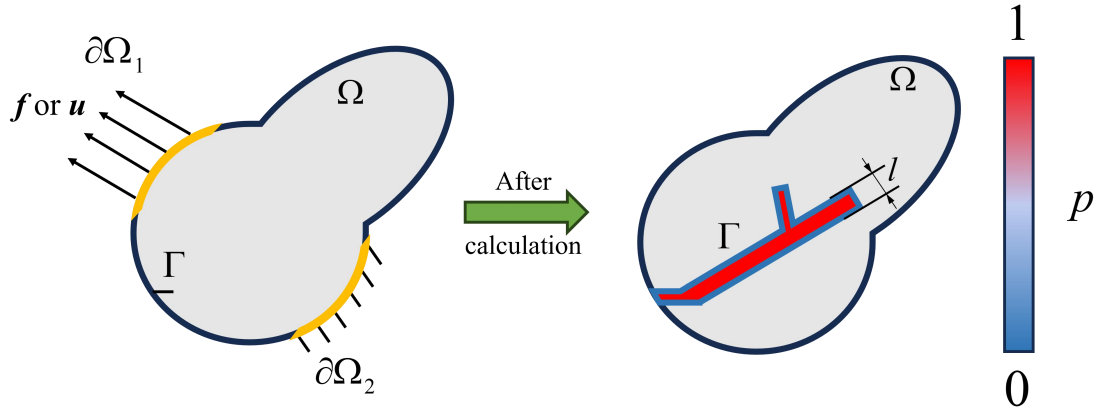


Fig. 7. Phase field approximation of the crack.

According to Griffith's theory [64], the energy required to create a fracture surface per unit area is equal to the critical fracture energy density G_c , also referred to as the critical energy release rate. Therefore, the total potential energy can be expressed as:

$$\psi_t = \int_{\Omega} \psi_{\varepsilon}(\boldsymbol{\varepsilon}) d\Omega + \int_{\Gamma} G_c dS - \int_{\Omega} \mathbf{b} \cdot \mathbf{u} d\Omega - \int_{\partial\Omega_1} \mathbf{f} \cdot \mathbf{u} dS \quad (19)$$

where the four terms are elastic energy, fracture energy, energy due to body forces, and energy due to external forces. The linear strain tensor $\boldsymbol{\varepsilon}$ is given by:

$$\varepsilon_{ij} = \frac{1}{2} \left(\frac{\partial u_i}{\partial x_j} + \frac{\partial u_j}{\partial x_i} \right) \quad (20)$$

Assuming isotropic linear elasticity, the elastic energy density function $\psi_{\varepsilon}(\boldsymbol{\varepsilon})$ is defined as presented by Miehe et al. [65].

$$\psi_{\varepsilon}(\boldsymbol{\varepsilon}) = \frac{1}{2} \lambda \cdot \text{tr}^2[\boldsymbol{\varepsilon}] + \mu \cdot \text{tr}[\boldsymbol{\varepsilon}^2] \quad (21)$$

where λ and μ are Lamé constants, which can be derived from Young's modulus and Poisson's ratio, and $\text{tr}[\mathbf{A}]$ represents the trace of the matrix \mathbf{A} .

Theoretically, the crack situation in the domain can be obtained by solving Eq. (19) through energy conservation. However, to solve for the crack distribution, some approximations and the concept of fields need to be introduced.

2.3.2 Phase field approach to fracture energy

By introducing a scalar phase field, brittle fracture can be successfully simulated [39]. A phase field $p(\mathbf{x}, t) \in [0, 1]$ is defined to approximate the fracture surface Γ . The phase field $p(\mathbf{x}, t) \in [0, 1]$ naturally represents a diffusive crack situation, where $p=1$ denotes the crack and $p=0$ indicates an uncracked body (as shown in Fig. 7). Therefore, the crack surface density per unit volume of the solid is given by Miehe et al. [65].

$$\gamma(p, \nabla p) = \frac{p^2}{2l_0} + \frac{l_0}{2} \cdot (\nabla p)^2 \quad (22)$$

where l_0 is a parameter that governs the transition region of the phase field from 0 to 1. This parameter, known as the length scale parameter, represents the width of the crack. By applying Eq. (22), the fracture energy can be approximated, transforming the originally complex surface integral into a domain integral, which facilitates the construction of phase field model.

$$\int_{\Gamma} G_c dS = \int_{\Omega} G_c \left[\frac{p^2}{2l_0} + \frac{l_0}{2} \cdot (\nabla p)^2 \right] d\Omega \quad (23)$$

Crack surface energy is driven by elastic energy, which controls the evolution of the phase field. To ensure crack propagation is only influenced by tensile loading, the elastic energy needs to be decomposed, with the compressive component having no contribution [39]. The method based on the spectral decomposition is as follows:

$$\boldsymbol{\varepsilon} = \boldsymbol{\varepsilon}_+ + \boldsymbol{\varepsilon}_- \quad (24)$$

$$\begin{cases} \boldsymbol{\varepsilon}_+ = \sum_{i=1}^d \langle \varepsilon_i \rangle_+ \mathbf{n}_i \otimes \mathbf{n}_i \\ \boldsymbol{\varepsilon}_- = \sum_{i=1}^d \langle \varepsilon_i \rangle_- \mathbf{n}_i \otimes \mathbf{n}_i \end{cases} \quad (25)$$

Where $\boldsymbol{\varepsilon}_+$ and $\boldsymbol{\varepsilon}_-$ are the tensile and compressive strain tensors; $\{\varepsilon_i\}_{i=1\dots d}$ are the principal strains and \mathbf{n}_i is its direction vector, respectively. The bracket operators

$$\text{mean } \langle x \rangle_+ = \frac{(x + |x|)}{2} \text{ and } \langle x \rangle_- = \frac{(x - |x|)}{2}.$$

In Eq. (19), the elastic energy density function ψ_{ε} represents the energy stored per unit volume in the bulk of the solid. Without considering damage, by applying the decomposed strain tensor from Eq. (25), the reference energy function associated with the undamaged elastic solid ψ_0 is similarly decomposed as follows [65]:

$$\psi_{\varepsilon 0} = \psi_{\varepsilon 0+} + \psi_{\varepsilon 0-} \quad (26)$$

$$\begin{cases} \psi_{\varepsilon 0+} = \lambda \cdot \frac{\langle \text{tr}[\boldsymbol{\varepsilon}] \rangle_+^2}{2} + \mu \cdot \langle \text{tr}[\boldsymbol{\varepsilon}_+^2] \rangle \\ \psi_{\varepsilon 0-} = \lambda \cdot \frac{\langle \text{tr}[\boldsymbol{\varepsilon}] \rangle_-^2}{2} + \mu \cdot \langle \text{tr}[\boldsymbol{\varepsilon}_-^2] \rangle \end{cases} \quad (27)$$

Considering crack propagation, with the assumption that only the tensile part of the elastic energy density is influenced by phase field, the degradation of energy due to fracture is incorporated, and finally, the elastic energy density function is then expressed as follows to model the stiffness reduction [66].

$$\psi_{\varepsilon}(\boldsymbol{\varepsilon}, p) = g(p) \psi_{\varepsilon 0+}(\boldsymbol{\varepsilon}) + \psi_{\varepsilon 0-}(\boldsymbol{\varepsilon}) \quad (28)$$

The monotonically decreasing degradation function $g(p)$ describes the degradation of the positive (tensile) part of the stored energy with evolving damage. It must satisfy the conditions: $g(0)=1$, $g(1)=0$, $g'(1)=0$. A common form of this function is a power function expressed as:

$$g(p) = (1-p)^2 \quad (29)$$

At this point, all terms in the potential energy can be expressed, and for a domain with kinetic energy, its kinetic energy can be represented as:

$$\int_{\Omega} \psi_{kin} d\Omega = \frac{1}{2} \int_{\Omega} \rho \left(\frac{\partial \mathbf{u}}{\partial t} \right)^2 d\Omega \quad (30)$$

The total Lagrange energy function is the sum of the fracture energy from Eq. (23), the elastic energy from Eq. (28), the kinetic energy from Eq. (30), and the external potential energy due to the applied loads.

$$L = \frac{1}{2} \int_{\Omega} \rho \left(\frac{\partial \mathbf{u}}{\partial t} \right)^2 d\Omega - \int_{\Omega} \left[(1-p)^2 \psi_{\varepsilon+} + \psi_{\varepsilon-} \right] d\Omega - \int_{\Omega} G_c \left[\frac{p^2}{2l_0} + \frac{l_0}{2} \cdot (\nabla p)^2 \right] d\Omega + \int_{\Omega} b_i u_i d\Omega + \int_{\partial\Omega_i} f_i u_i dS \quad (31)$$

By applying the variational principle to the function L , the first variation must be zero [39], which results in the governing equations:

$$\begin{cases} \frac{\partial \sigma_{ij}}{\partial x_j} + b_i = \rho \frac{\partial^2 u}{\partial t^2} \\ \left(\frac{2l_0 \psi_{\varepsilon+}}{G_c} + 1 \right) \cdot p - l_0^2 \nabla^2 p = \frac{2l_0 \psi_{\varepsilon+}}{G_c} \end{cases} \quad (32)$$

where σ_{ij} is the component of Cauchy stress tensor, which can be similarly decomposed, given as:

$$\sigma_{ij} = (1-p)^2 \frac{\partial \psi_{\varepsilon+}}{\partial \varepsilon_{ij}} + \frac{\partial \psi_{\varepsilon-}}{\partial \varepsilon_{ij}} \quad (33)$$

and Cauchy stress tensor can be rewritten.

$$\boldsymbol{\sigma} = (1-p)^2 \left[\lambda \langle tr(\boldsymbol{\varepsilon}) \rangle_+ \mathbf{I} + 2\mu \boldsymbol{\varepsilon}_+ \right] + \lambda \langle tr(\boldsymbol{\varepsilon}) \rangle_- \mathbf{I} + 2\mu \boldsymbol{\varepsilon}_- \quad (34)$$

where \mathbf{I} is a unit tensor $\in \mathbb{R}^{d \times d}$.

However, if the above phase-field model is applied directly, the phase field would recover or even vanish after the load is removed, which contradicts the irreversibility of cracks in real materials. To ensure a monotonically increasing phase field, an irreversibility condition must be imposed before calculating. Therefore, a strain-history field $H(\mathbf{x}, t)$ is introduced to record the maximum value of the elastic energy density [67].

$$H(\mathbf{x}, t) = \max_{s \in [0, t]} \psi_{\varepsilon+}[\boldsymbol{\varepsilon}(\mathbf{x}, s)] \quad (35)$$

Replacing $\psi_{\varepsilon+}$ by $H(\mathbf{x}, t)$ in Eq. (32), the second-order PDE in the strong form of the phase field model is obtained.

$$\left(\frac{2l_0 H}{G_c} + 1 \right) \cdot p - l_0^2 \nabla^2 p = \frac{2l_0 H}{G_c} \quad (36)$$

2.3.3 Weak form for FEM and solution strategy

The phase-field modeling in this work involves a coupled multi-physics problem, with displacement and phase-field as the two primary fields, along with the strain-history variable H . The displacement field is solved using the "Solid Mechanics" module in COMSOL, while the phase field is governed by the energy conservation equation. To apply the finite element method for solving, the governing equations need to be reformulated into their weak form [39 and 41]:

$$\int_{\Omega} \left(-\rho \frac{\partial^2 \mathbf{u}}{\partial t^2} \cdot \delta \mathbf{u} - \boldsymbol{\sigma} : \delta \boldsymbol{\varepsilon} \right) d\Omega + \int_{\Omega} \mathbf{b} \cdot \delta \mathbf{u} d\Omega + \int_{\partial\Omega_i} \mathbf{f} \cdot \delta \mathbf{u} dS = 0 \quad (37)$$

where δ represents the test function in FEM, and

$$\int_{\Omega} l_0 H g'(p) \delta p d\Omega + \int_{\Omega} G_c \left[l_0^2 \cdot \nabla p \cdot \nabla (\delta p) + p \cdot \delta p \right] d\Omega = 0 \quad (38)$$

To avoid the unacceptable computational cost of fully coupled calculations, this study adopts a decoupled solver to sequentially solve for the displacement field, history strain field, and phase field (as shown in Fig. 3), thereby enabling reasonable simulation of the crack.

Finally, as for the phase-field parameters of the outer three coatings of the TRISO particle, the length scale parameters for PyC and SiC are assumed to be $l_1=3 \mu\text{m}$ and $l_2=1 \mu\text{m}$, respectively. The critical energy release rate, G_c , can be derived using the formula proposed by Borden et al. [66]:

$$G_c = \frac{256}{27} \cdot \frac{\sigma_c^2 l_0}{E} \quad (39)$$

where σ_c is the tensile strength (critical fracture stress), which can be experimentally tested as 200 MPa for PyC [68] and 667 MPa for SiC [59]; E is Young's modulus, which can be dynamically calculated from Eq. (6) and Eq. (7). The anisotropic PyC's E in this formula is represented by the average value in the three directions.

3. Verification

The code has been validated against a IAEA HTGR benchmark, specifically the Case-8 scenario from the IAEA Coordinated Research Program (CRP-6) [69]. This case was selected to verify the accuracy of the computational method by modeling the

outer three coatings of the TRISO particles subjected to ten time cycles, each lasting 100 days. In each cycle, the fuel temperature increases linearly from the initial 873 K to 1273 K, followed by an immediate drop back to 873 K. Meanwhile, the gas pressure on the inner side of the IPyC layer also increases and decreases linearly within each cycle. The results of the maximum tangential stresses at the inner surface of IPyC and SiC were compared with those obtained from other programs, demonstrating a good agreement with the results from different codes. This indicates that the software in this study can accurately simulate the mechanical performance of TRISO particles. Meanwhile, the thermomechanical properties of the entire TRISO particle were also compared with the results from the BISON program, validating the reliability of the simulation for the TRISO particle. Detailed results can be found in our previous study [20].

To validate the phase-field calculation method, two typical test cases are selected. First, for a square plate with an initial notch subjected to static tension loading, as shown in Fig. 8, a vertical displacement u_y is applied to the upper boundary of the plate, with u_x . The material parameters are: $E=210$ GPa, $\nu=0.3$, $Gc=2700$ J/m², and the length scale parameter $l_0=1.5\times10^{-2}$ mm. The maximum element size h is set to $l_0/2$. A displacement increment of $\Delta u=1\times10^{-5}$ mm is applied for the initial 450 time steps, followed by a smaller increment $\Delta u=1\times10^{-6}$ mm for the remaining time steps, until the material fully fractures.

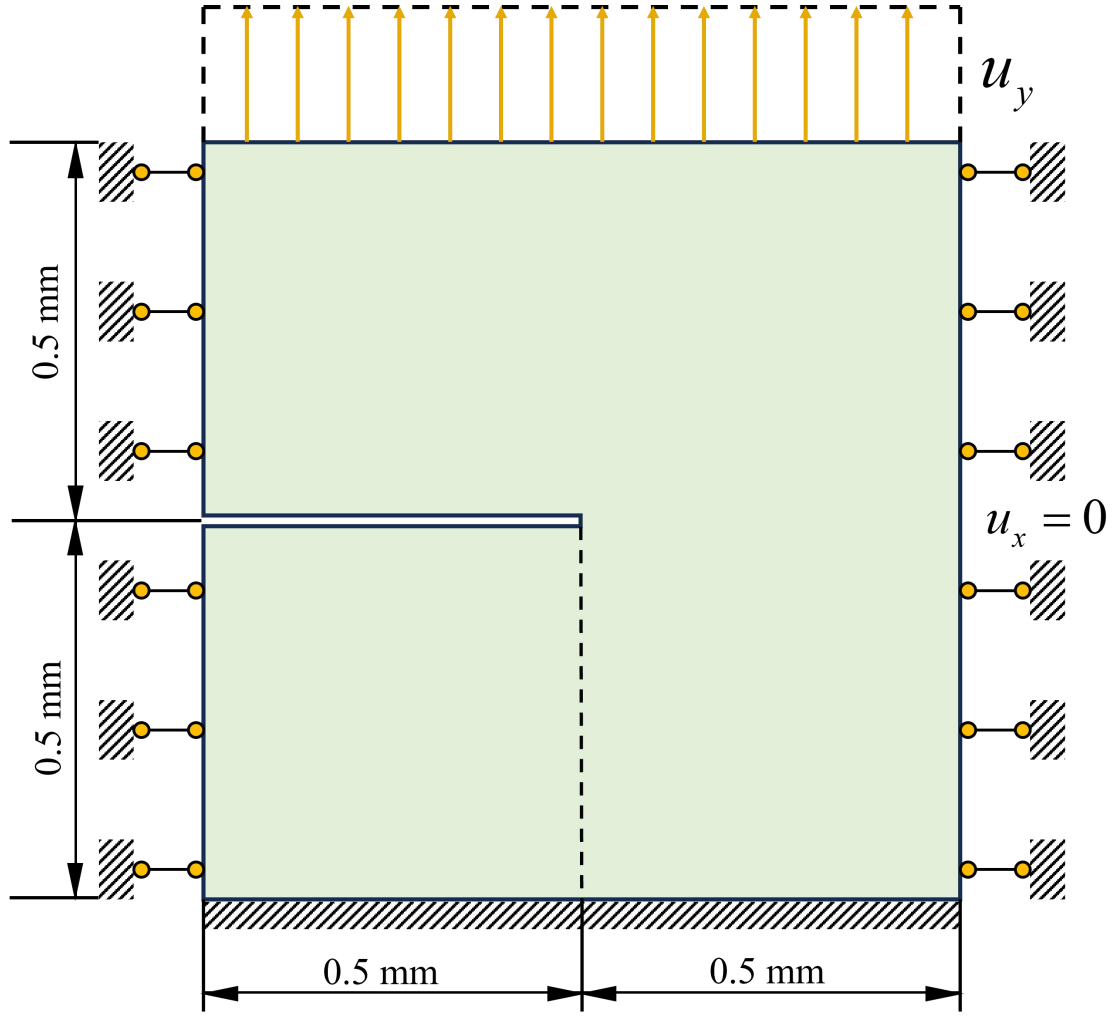


Fig. 8. Geometry and conditions for plate with an initial notch subjected to tension.

The computational results for this test case are presented in Fig. 9. As the tensile displacement increases, stress concentrates at the notch, and the crack gradually forms and propagates. The results show excellent agreement with the results by S. Zhou et al [39].

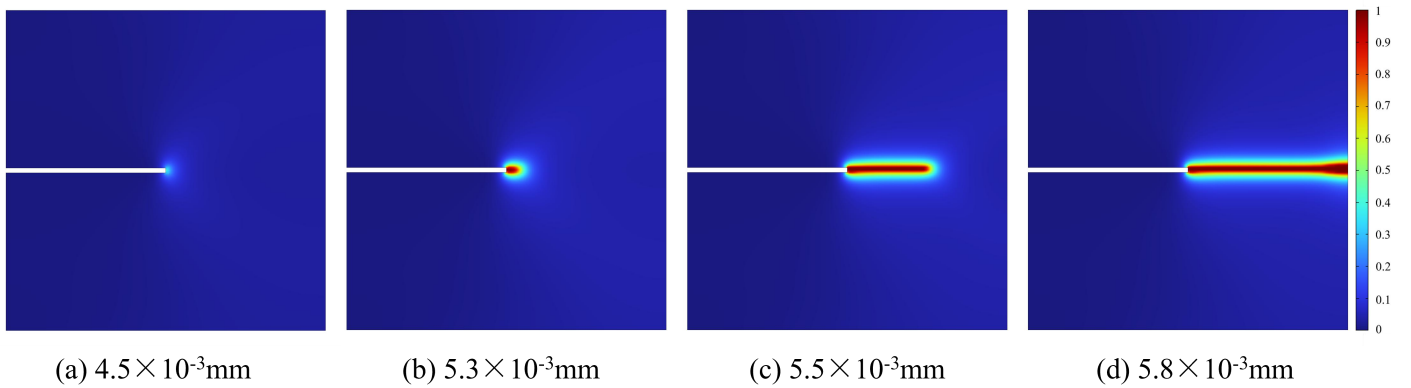


Fig. 9. Phase field of the plate subjected to tension at different displacements

u_y .

To further verify the accuracy of transient calculations and phase-field modeling

under shear forces, this study also selects the Kalthoff dynamic fracture experiment for comparison [70]. In this experiment, a steel plate with pre-existing cracks is placed freely on an adjustable workbench. A stress wave is generated by edge impact loading, which causes edge cracks and initiates brittle fracture. Based on the Kalthoff experiment, a computational problem for numerical simulation is constructed, as shown in Fig. 10.

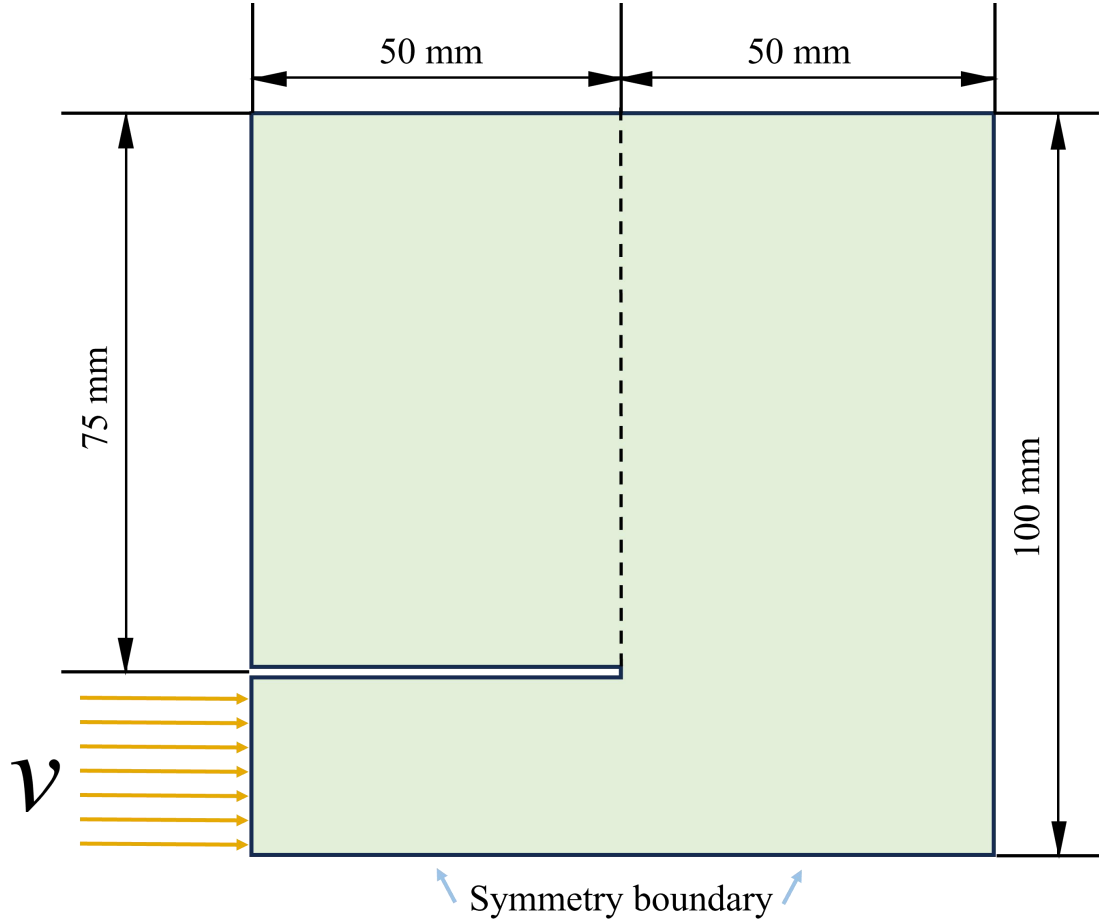


Fig. 10. Geometry and boundary conditions of Kalthoff experiment.
The specified velocity v is set as:

$$v = \begin{cases} \frac{t}{t_0} v_0 & t \leq t_0 \\ v_0 & t > t_0 \end{cases} \quad (40)$$

where v_0 is 16.5m/s and t_0 is 1 μ s. The material property are: $\rho = 8000\text{kg/m}^3$, $E = 190\text{ GPa}$, $\nu = 0.3$, and $G_c = 22130\text{ J/m}^2$, $l_0 = 3.9 \times 10^{-4}\text{ m}$. Next, the simulation is computed up to 90 μ s, and the phase field results at several time points are shown in Fig. 11. The crack appears at 24.84 μ s and gradually extends upward towards the top of the plate. The crack angle relative to the horizontal axis is approximately 65 degrees, which is consistent with the conclusions in [39] (ranging from 63° to 67°) and similar to the experimental results in [70]. Additionally, the cracks simulated using XFEM [71] and the phantom nodes method [72] from other studies are shown

in Fig. 13. It is evident that the crack obtained using the phase field model in this study is very similar to these results, demonstrating that the phase field approach developed in this study for brittle fracture is reliable.

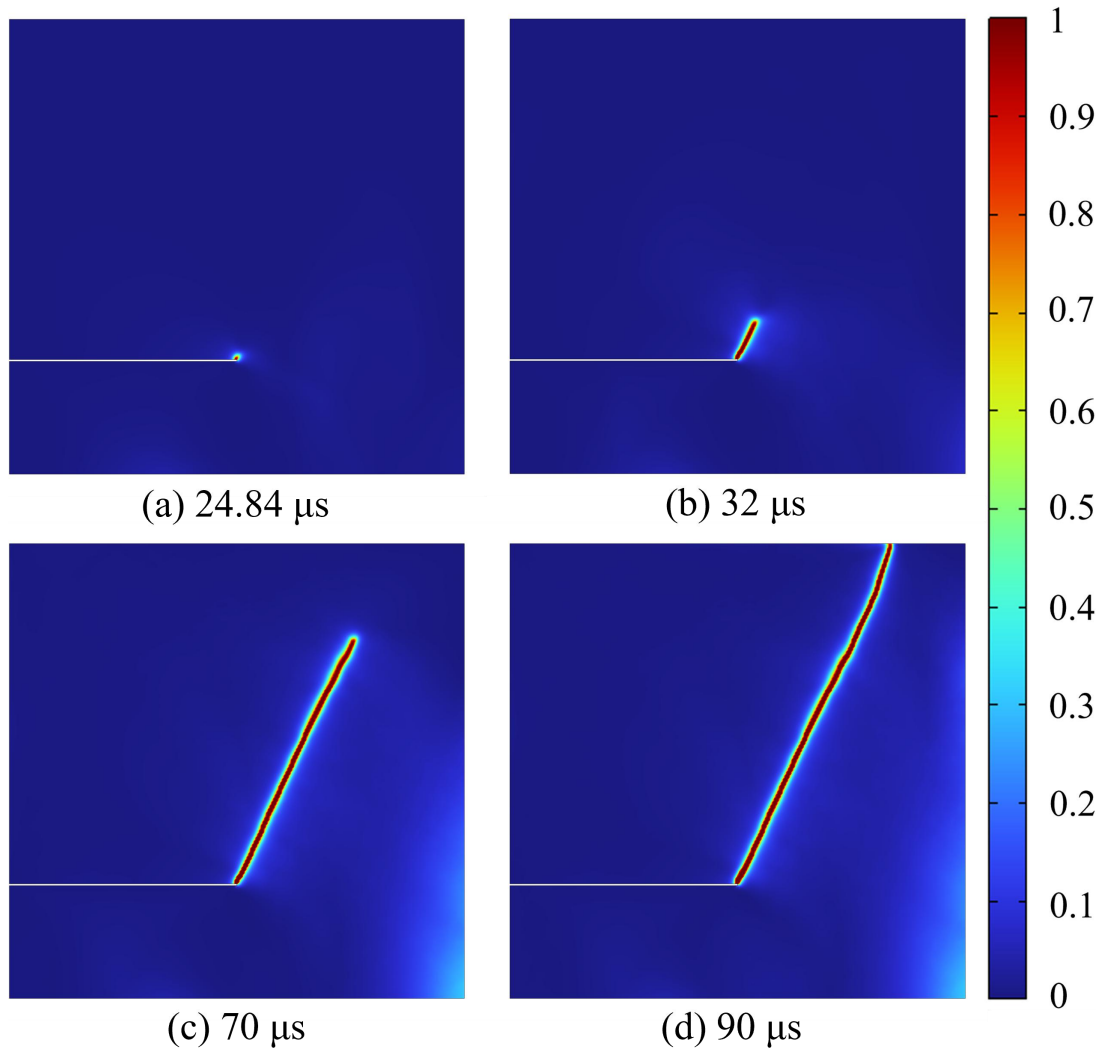
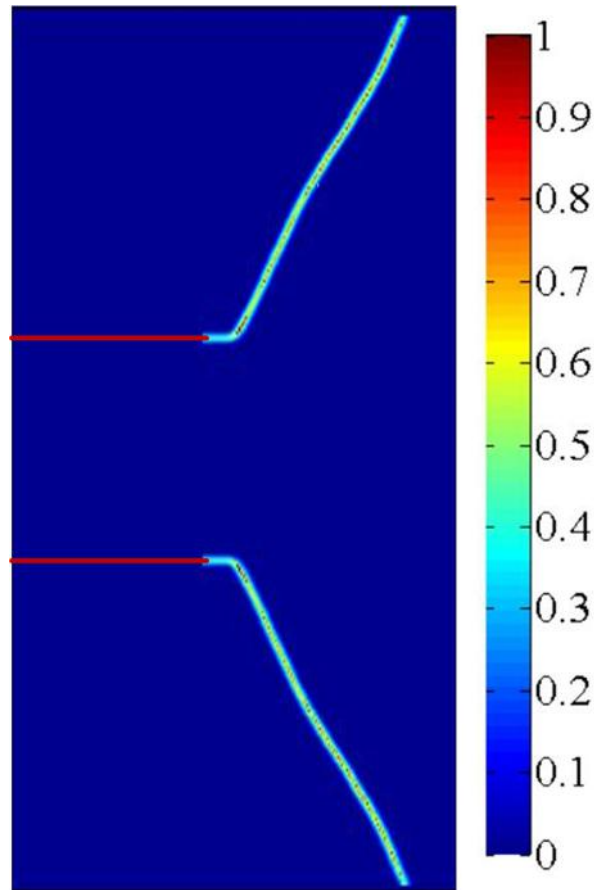
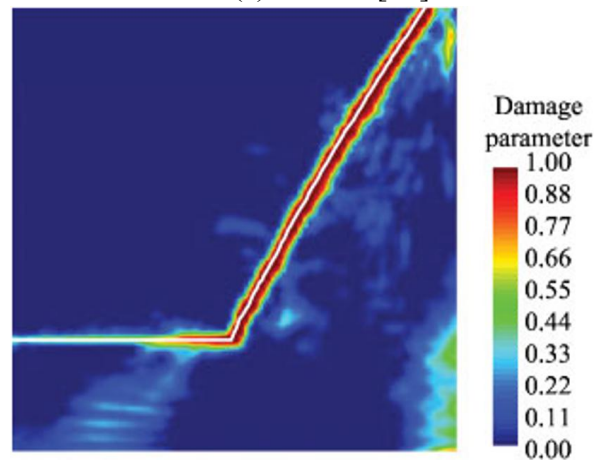


Fig. 11. Phase field at different time steps in the Kalthoff problem.



(a) XFEM [71].



(b) Phantom nodes method [72].

Fig. 12. Crack simulation results calculated using other methods [71 and 72].

4. Demonstration problems

Cracks may be left during manufacturing or generated during use in the PyC layer [40 and 73], while residual pores are prone to exist in the SiC layer [74 and 75]. These irregular geometries can lead to stress concentration, significantly affecting the TRISO particles and potentially causing the coating to fracture. Therefore, studying these features is crucial for the practical application of TRISO particles. This study analyzes four scenarios: 1) a crack on the inner side of the IPyC layer, 2) a residual

pore in the SiC layer, 3) a crack on the outer side of the OPyC layer, and 4) the combined effect of crack on the inner side of the IPyC layer and a residual pore in the SiC layer. Since IPyC and SiC are not monolithic, debonding may occur between them. When a crack reaches the interface between them, it tends to deflect in both directions [76]. Therefore, in the geometric model, a thin layer of $0.8\ \mu\text{m}$ is defined on the outer side of IPyC and the inner side of OPyC, with their critical energy release rate G_c set to 0.8 times that of PyC, in order to simulate the interfacial damage between the two layers. The geometric models for these features are shown in Fig. 13. Irradiation behavior is incorporated into the model, with the IPyC layer subjected to fission gas pressure. Meanwhile, to ensure both the accuracy and convergence of the calculations, the pressure is linearly removed once the crack reaches the outer side of the OPyC layer. Otherwise, the separated materials would move too far apart.

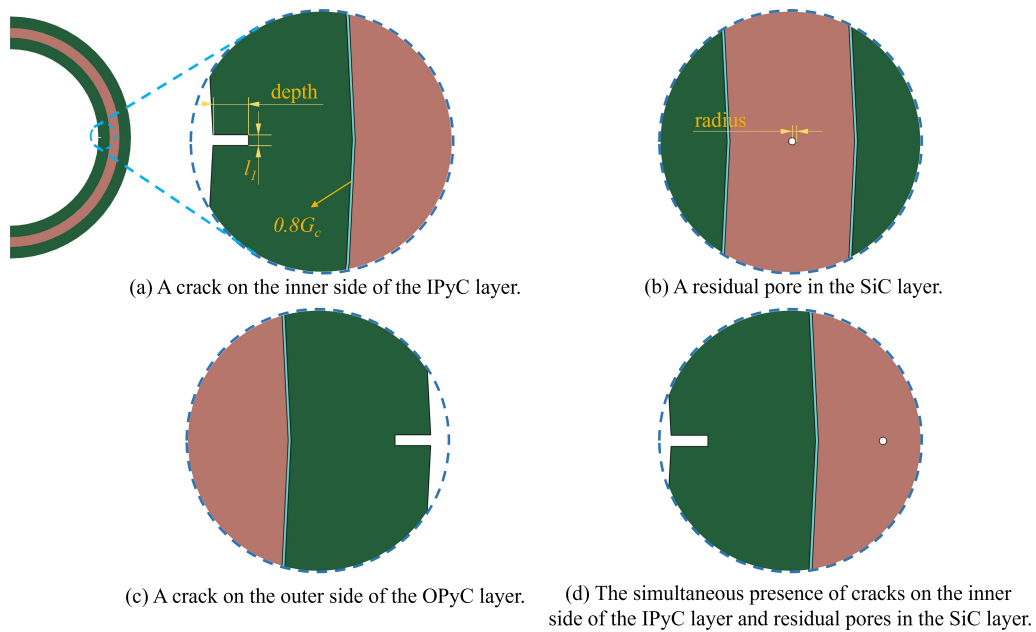


Fig. 13. Four geometric models used to simulate the effects of cracks and residual pores in TRISO particle coatings.

Moreover, to investigate the sensitivity of crack propagation characteristics in the outer three coatings of TRISO particles to geometric parameters, and to provide recommendations for the required limitations on pre-existing crack sizes in practical engineering applications for TRISO particles, this study parameterized the depth of the crack and the radius of the pore in scenarios 1 and 2. The parameters used for this analysis are listed in Table 1. And because the SiC layer is highly reliable under normal operating conditions, scenarios 1 and 3 are modeled using typical HTGR conditions [14 and 77], while scenarios 2 and 4 are modeled using more stringent space reactor conditions [20]. The corresponding parameters are listed in Table 2.

Table 1. Parameters used for the geometric models in different scenarios.

Scenario	Geometric parameters	
	Crack depth (μm)	Pore radius (μm)
1 (IPyC)	1, 3, 5, 5.6, 5.7, 5.8, 5.9, 6, 8, 10	-

2 (SiC)	-	0.1, 0.2, 0.4, 0.6, 0.7, 0.75, 0.8, 0.85, 0.9, 1
3 (OPyC)	10	-
4 (IPyC & SiC)	10	1

Table 2. Parameters for the two conditions used in simulations [14, 20 and 77].

Parameter	Value	
	HTGR	Space reactor
Applied scenarios	1 and 3	2, 3 and 4
Kernel power	50 mW	70 mW
Lifetime of fuel	76 Ms (About 2.4 yrs.) (Scenario 1 calculated up to 15 Ms only)	220 Ms (About 7 yes.)
TRISO particle temperature	1500 K	1700 K
Fast neutron flux	5×10^{17} n/m ² /s	7×10^{17} n/m ² /s
Fast fluence at the end of irradiation	3.8×10^{25} n/m ²	15.4×10^{25} n/m ²
Fission rate per unit volume	3.03×10^{19} fission/m ³ /s	4.24×10^{19} fission/m ³ /s
Burnup at the end	10.45% FIMA	42.35% FIMA
Gas pressure	As shown in Fig. 6	

5. Results and discussion

5.1 Effect of a crack in the IPyC layer

The irradiation behavior is most active before 1.5×10^7 s (as shown in Fig. 5), and the maximum tangential stress in the IPyC layer also occurs before this time. After this point, as the burnup progresses, the stress gradually relaxes [20]. Therefore, crack formation and propagation primarily occur during the early stages of burnup. If no cracks form by this time, no cracks will appear in the subsequent stages. Consequently, the maximum calculation time is set to 1.5×10^7 s.

Figs. 14, 15, and 16 show the phase field at selected time points for pre-existing cracks of 1 μ m, 6 μ m, and 10 μ m in depth in the IPyC inner side. When a 1 μ m deep crack is present, the stress distribution within the IPyC layer remains relatively uniform, with no significant effect from the crack, and the maximum phase field value at the end of the calculation is only 0.17, indicating no crack propagation. However, when a 6 μ m deep crack exists, the crack begins to propagate towards the SiC layer at 0.80×10^7 s, and upon reaching the interface, it deflects in both directions, leading to debonding between the IPyC and SiC layers. With a 10 μ m deep crack, crack propagation starts earlier, at 0.43×10^7 s. The crack expands more rapidly after reaching the interface, and by 1.50×10^7 s, most of the region on the outer side of the IPyC layer has separated from the SiC layer.

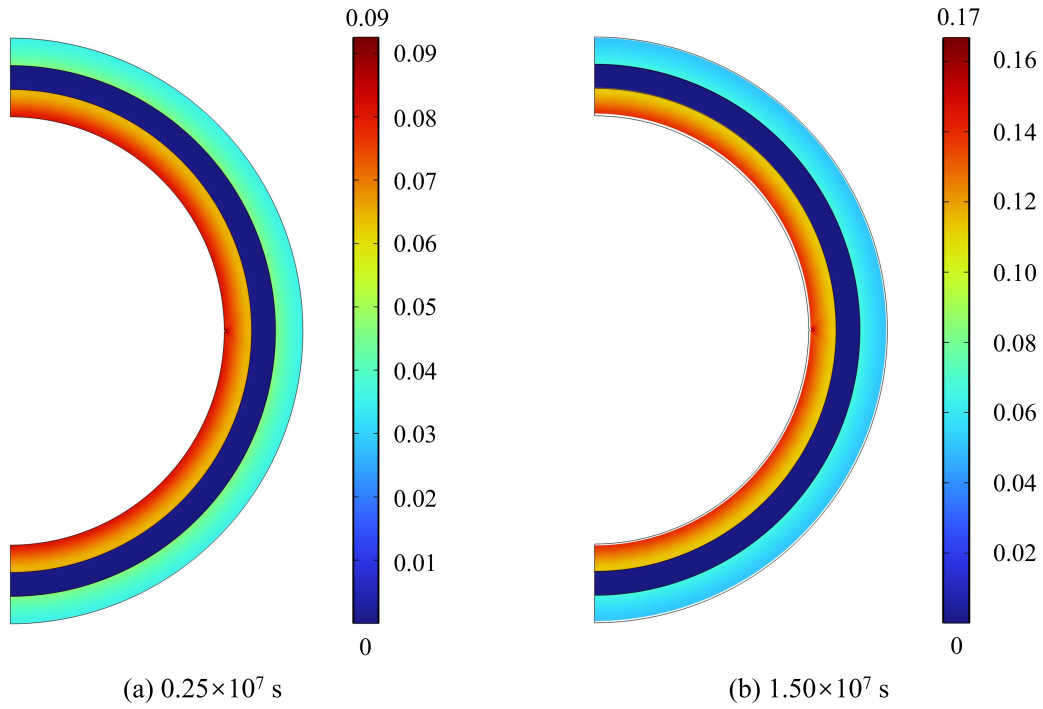


Fig. 14. Phase field for a 1 μm deep crack on the inner side of the IPyC layer.

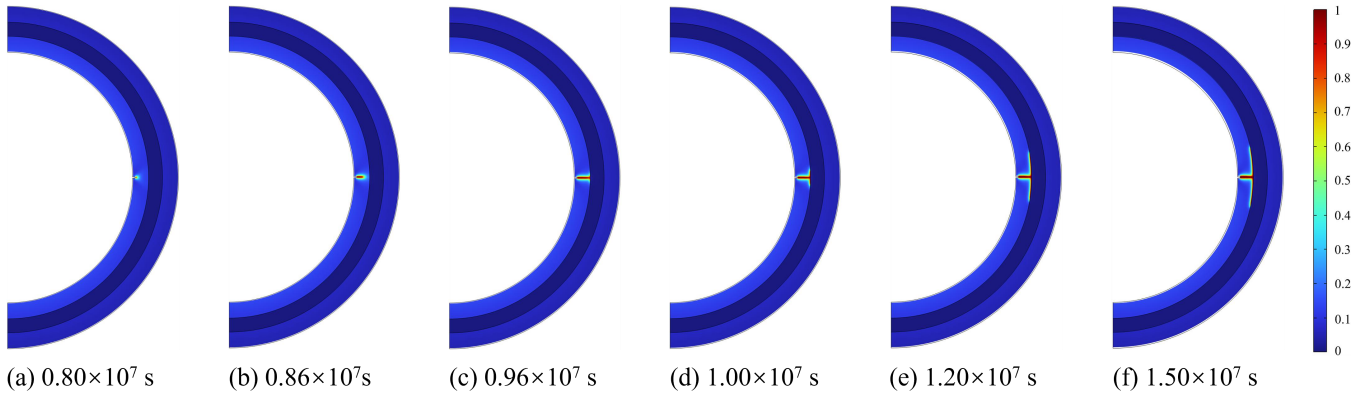


Fig. 15. Phase field for a 6 μm deep crack on the inner side of the IPyC layer.

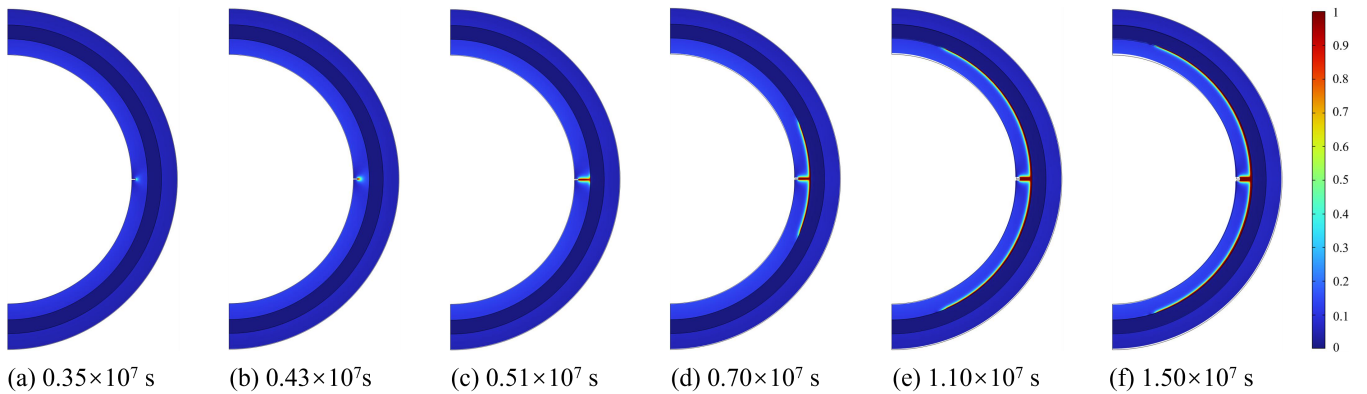


Fig. 16. Phase field for a 10 μm deep crack on the inner side of the IPyC layer.

Fig. 17 shows the maximum phase field values at 1.5×10^7 s and the times when cracks start to propagate (if propagation occurs) for different pre-crack depths. When the crack depth is smaller than 5.8 μm , no crack propagation occurs. However, when the crack depth is sufficient, the crack will propagate, and the time at which

propagation begins becomes earlier as the pre-crack depth increases.

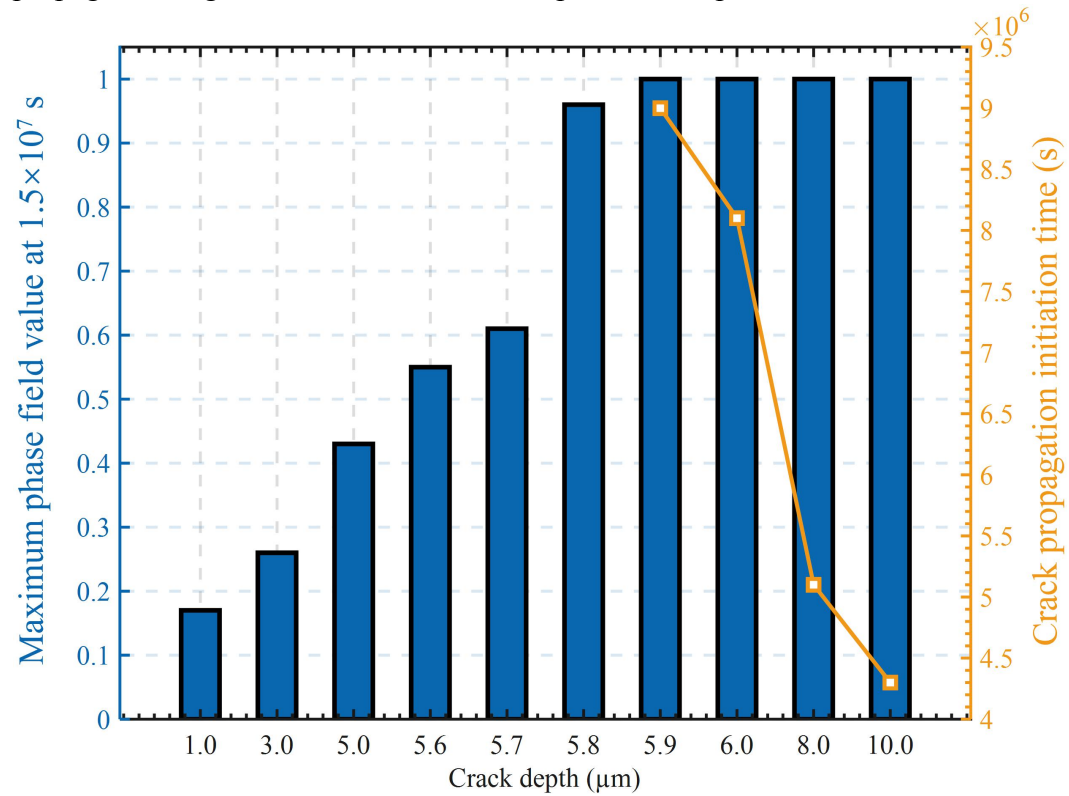


Fig. 17. Maximum phase field values at 1.5×10^7 s and crack propagation initiation times for different pre-crack depths.

Fig. 18 presents the tangential stress (hoop stress) distribution at 1.5×10^7 s for pre-existing cracks with depths of 5 μm, 6 μm, and 10 μm. When the crack does not propagate, the notch induces significant tensile stress in the IPyC layer, while the SiC layer remains under compressive stress. In the case of a 6 μm pre-existing crack, the local debonding between the IPyC and SiC layers caused by crack propagation results in a strong compressive stress concentration in the SiC layer beyond the crack tip due to the constraint exerted by the IPyC layer. In contrast, the region near the crack front experiences tensile stress. Fortunately, this tensile stress concentration is primarily confined within the IPyC layer, and the localized tensile stress is not sufficient to cause fracture in the SiC layer.

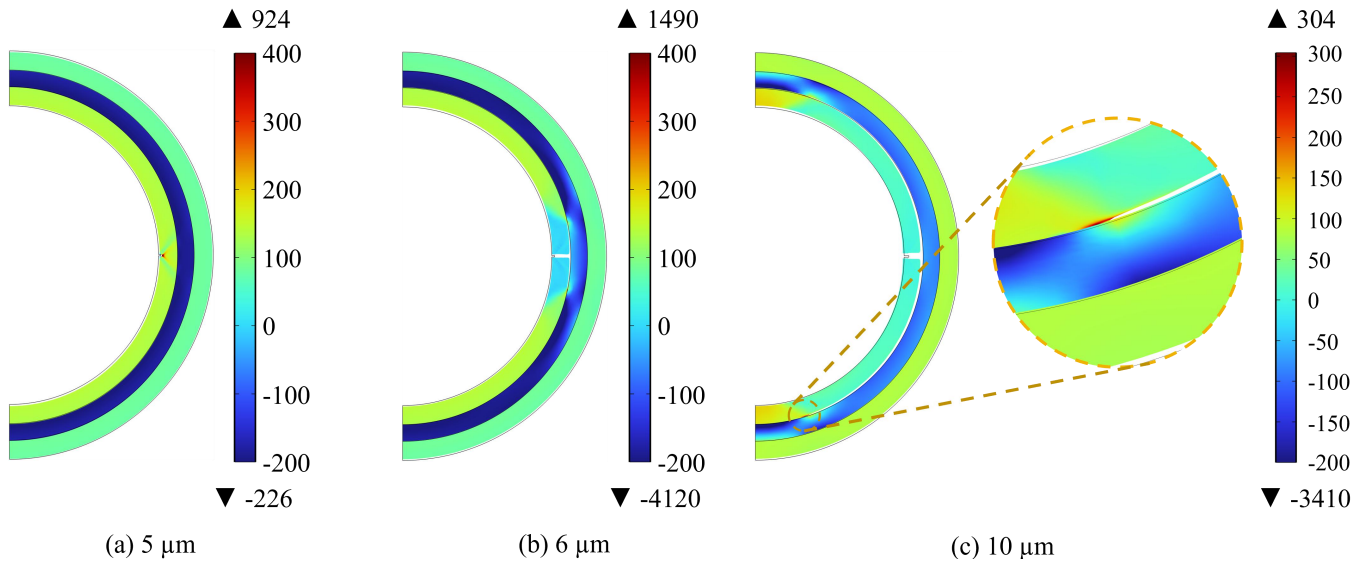


Fig. 18. Tangential stresses for 5 μm , 6 μm and 10 μm deep pre-crack on the inner side of the IPyC layer.

As for the effects of IPyC cracks and interface debonding on SiC stress, Fig. 19 shows the proportions of debonded area and the maximum tangential (hoop) stress in the SiC layer at the end of the calculation for different pre-crack depths. Overall, cracks in the IPyC layer increase the tensile stress experienced by the SiC layer. When crack propagation does not occur, the SiC layer remains under compressive stress at the end of the burnup. Once a crack forms, the stress concentration caused by interface debonding and the crack tip causes the SiC to experience tensile stress at the same time. Deeper pre-cracks lead to cracks propagating further along the interface, and while more debonding at the interface can alleviate the tensile stress in SiC, the stress remains significantly higher than when crack propagation does not occur.

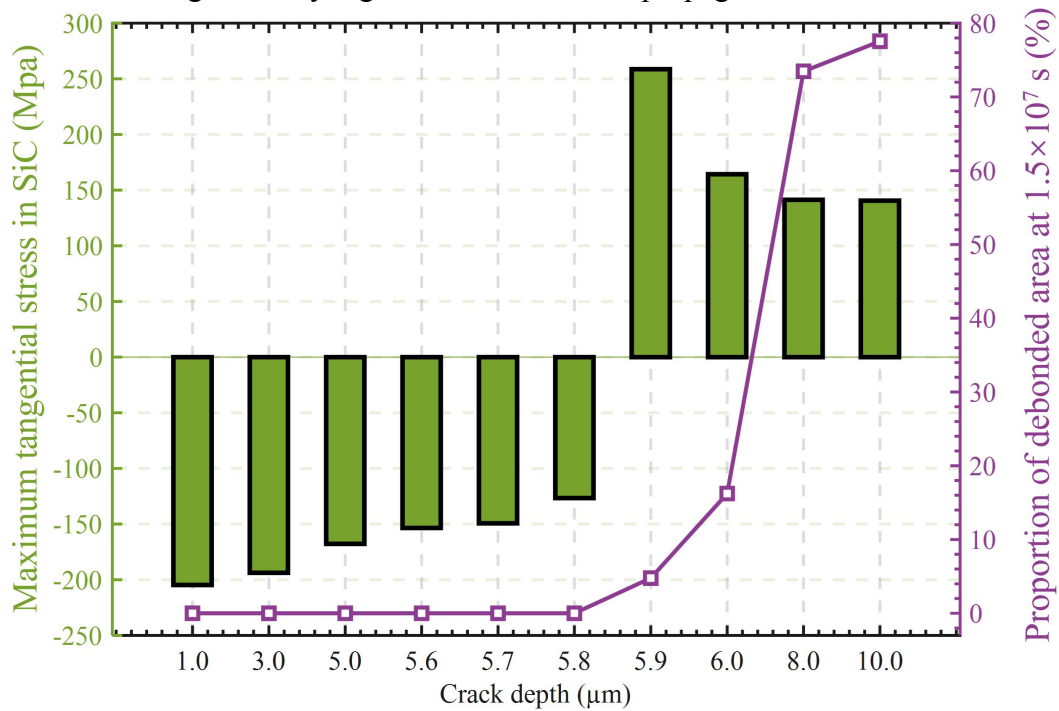


Fig. 19. Proportions of debonded area and maximum tangential stress in SiC for

different pre-crack depths.

For a 10 μm pre-crack, its behavior throughout the fuel lifetime has been simulated, and Fig. 20 compares the maximum tangential stress on the inner surface of SiC layer with and without the pre-existing crack. When the crack gets close to the inner side of SiC, it induces a sudden increase in tensile stress within the SiC layer. Since SiC has significantly higher strength than pyrolytic carbon and the stress concentration occurs in a very localized region, no immediate cracking occurs in the early stages of burnup. However, at $7.6 \times 10^7 \text{s}$, the maximum tangential stress in the SiC layer becomes significantly higher than in the case without an initial crack in the IPyC. This could have a considerable impact in long-lifetime applications, such as space nuclear reactors.

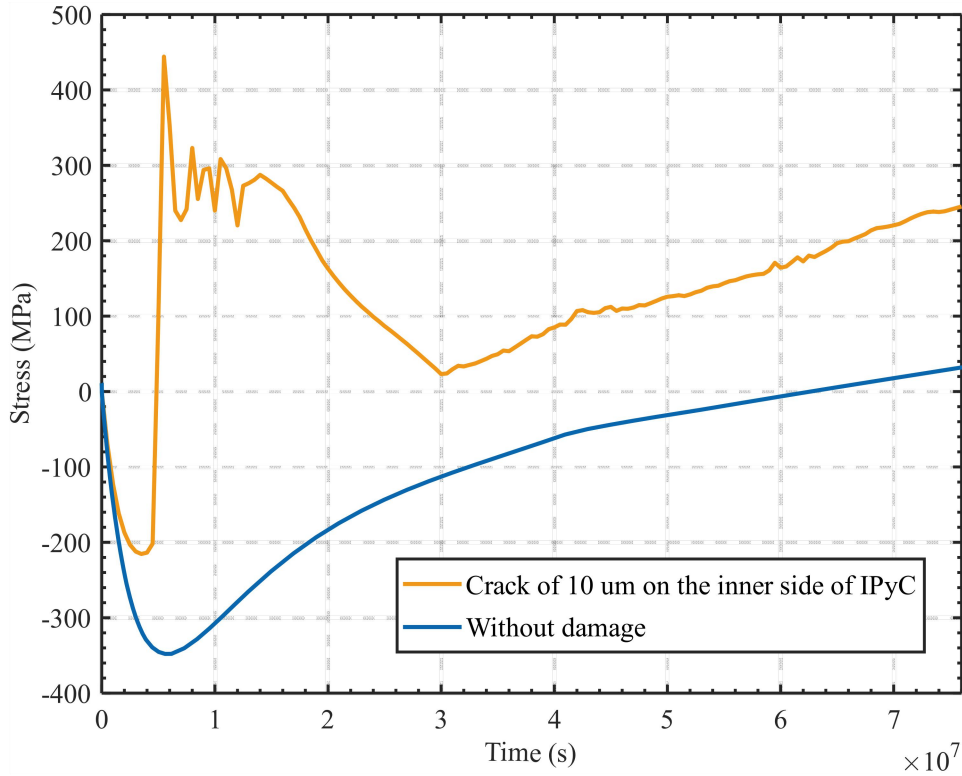


Fig. 20. Comparison of tangential stress on the inner surface of SiC layer with and without a 10 μm pre-crack on the inner side of IPyC.

5.2 Effect of a residual pore in the SiC layer

SiC with residual pores of 0.1 μm and 1 μm radii at different time points are shown in Figs. 21 and 22, respectively. When a 0.1 μm pore is present, there is no significant stress concentration around the pore, and no individual crack forms. Instead, the SiC layer is pulled apart by the excessive internal pressure from the IPyC layer, leading to the failure of the coating. In contrast, with a 1 μm pore, the impact of this geometric defect on the SiC stress is more pronounced, causing cracks to form on both sides of the pore and propagate inwards and outwards, eventually resulting in the complete fracture of all three coatings.

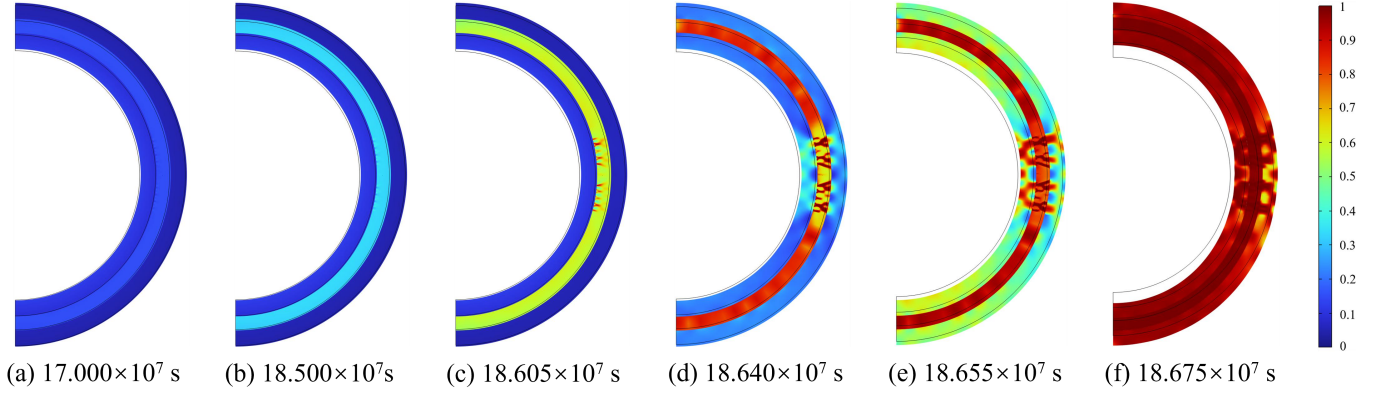


Fig. 21. Phase field with a residual pore of $0.1 \mu\text{m}$ radius in SiC.

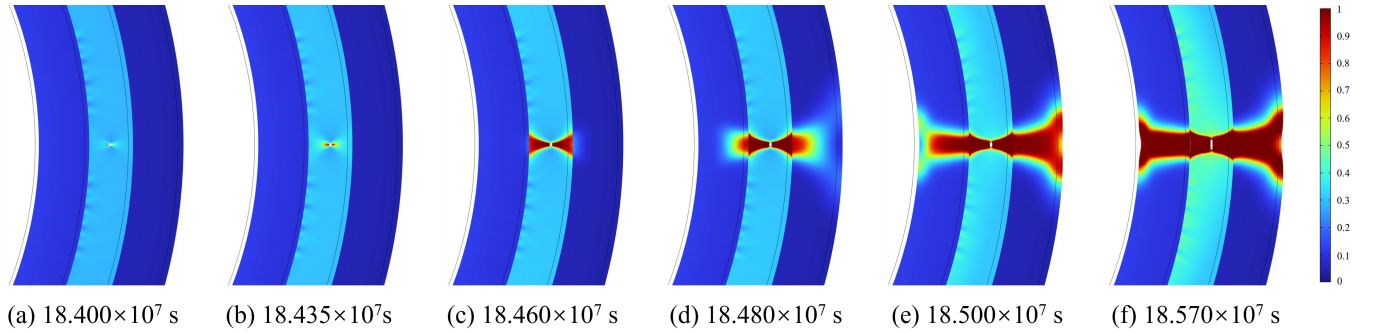


Fig. 22. Phase field with a residual pore of $1 \mu\text{m}$ radius in SiC.

Fig. 23 shows the complete fracture time of the outer three coatings and the gas pressure on the inner side of the IPyC layer at fracture for different sizes of residual pores in SiC. It is observed that with a larger pore radius, the time to complete fracture occurs slightly earlier. When the pore radius exceeds $0.2 \mu\text{m}$, the pore begins to have an impact on the overall structure of SiC. However, the impact of residual pores in SiC on the structural strength of TRISO particles is not very significant. Even with a $1 \mu\text{m}$ residual pore, the outer three coatings still fracture after more than five and a half years. Therefore, the fracture of SiC is primarily due to excessive fission gas pressure rather than residual pores. In the model in this study, the gas pressure that TRISO particles can withstand should not exceed 139 MPa.

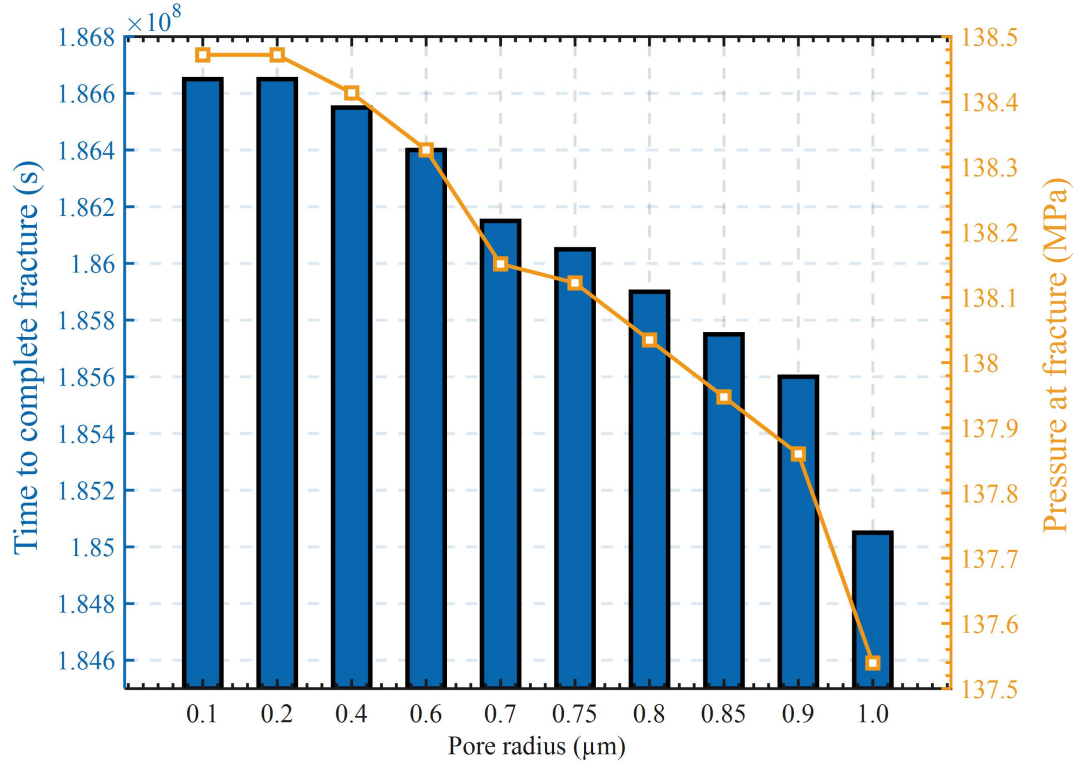


Fig. 23. Time to complete fracture and gas pressure at fracture under different residual pores in SiC.

5.3 Effect of a crack in the OPyC layer

The HTGR conditions were first applied to simulate the impact of this type of crack. Fig. 24 and 25 present the phase field and tangential stress distribution at 7.6×10^7 s for a 10 μm deep pre-crack on the outer side of the OPyC layer, as well as the comparison of tangential stress on the inner surface of the SiC layer, respectively. Although this type of pre-crack induces stress concentration at its tip, the maximum phase field value remains only 0.28 at the end of the fuel lifetime. The tangential stress on the inner surface of the SiC layer is higher than in the case without a crack throughout the entire lifetime, but its impact is weaker compared to the pre-crack on the inner side of the IPyC layer. However, as shown in Fig. 24(b), due to the radial shrinkage of the pyrolytic carbon under irradiation, the tensile stress transmitted to the outer surface of the SiC layer may cause fracture initiation from the outer side. Therefore, the potential impact of this type of crack on TRISO particles under space reactor conditions is further investigated.

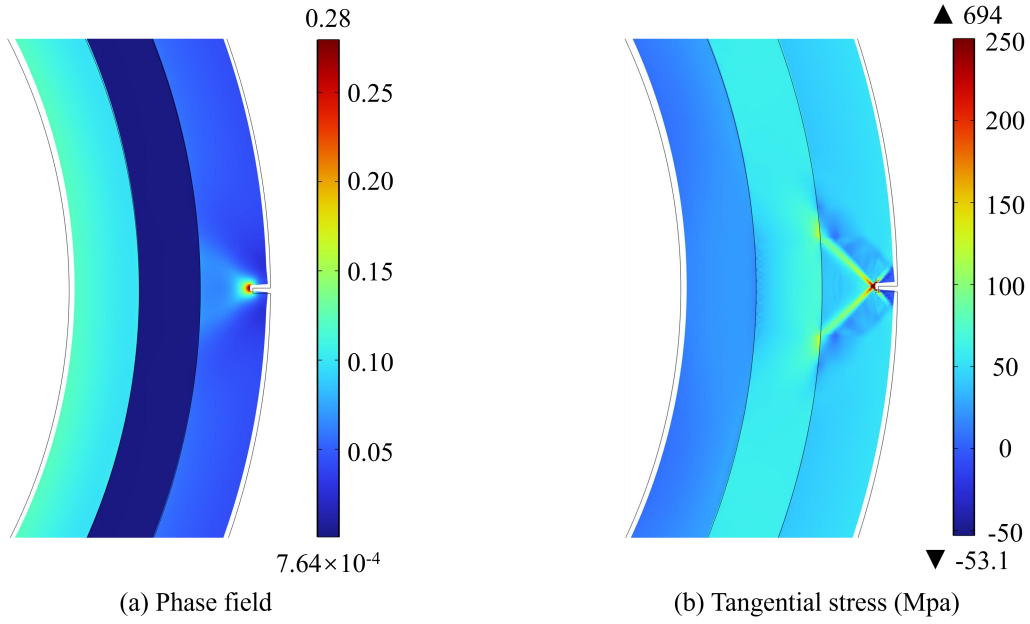


Fig. 24. Phase field and tangential stress at 7.6×10^7 s with a $10 \mu\text{m}$ deep pre-crack on the outer side of OPyC under HTGR conditions.

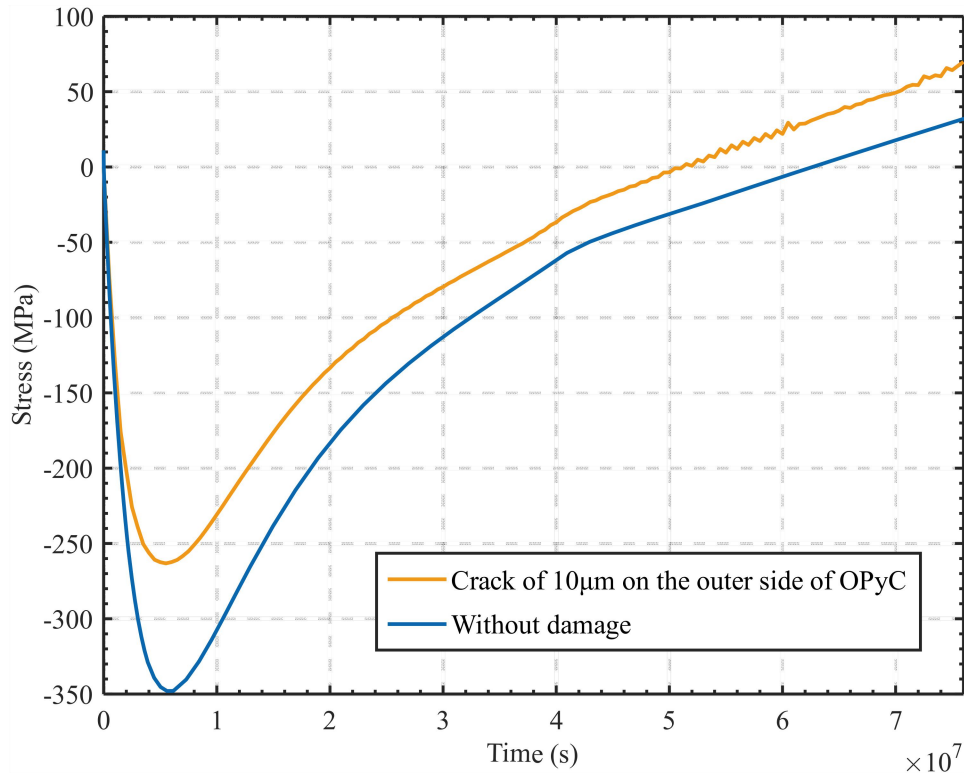


Fig. 25. Comparison of tangential stress on the inner surface of the SiC layer with and without a $10 \mu\text{m}$ pre-crack on the outer side of OPyC.

Under space reactor operating conditions, the phase field with a pre-crack on the outer side of the OPyC layer is shown in Fig. 26. Unlike the crack on the inner side of the IPyC layer, this type of crack remains highly stable throughout the early and mid-burnup stages. Although the crack slightly expands, the inward shrinkage of OPyC is supported by the SiC layer, which does not lead crack propagation until 18×10^7 s. At 18.155×10^7 s, due to the tensile stress concentration at two locations on

the outer surface of the SiC layer, as shown in Fig. 24(b), two corresponding cracks first initiate and propagate inward through the SiC layer. This crack propagation path is similar to those observed in crack paths in ceramic laminates [78]. By 18.200×10^7 s, both cracks fully penetrate the SiC and IPyC layers, leading to a complete fracture of the TRISO particle's outer coating layers. This occurs earlier than in the case where a $1 \mu\text{m}$ radius residual pore exists in the SiC layer, but both scenarios result in the complete failure of the outer coating layers only at the very end of the burnup process.

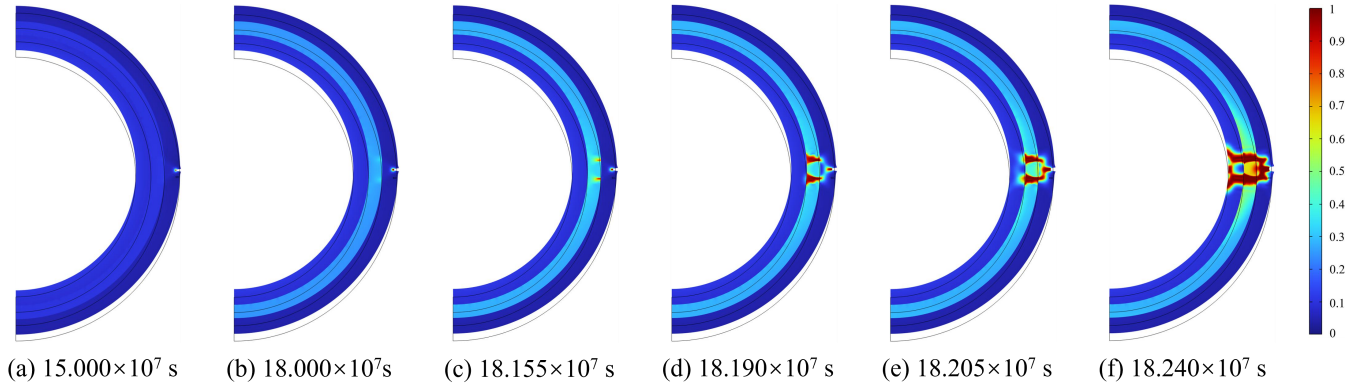


Fig. 26. Phase field with a $10 \mu\text{m}$ pre-crack on the outer side of OPyC under space reactor conditions.

5.4 Combined effect of a crack in the IPyC layer and a residual pore in the SiC layer

Simulated crack propagation results for a crack in the IPyC layer and a residual pore in the SiC layer are shown in Fig. 24. During the early stages of burnup, the crack in the IPyC layer extends and causes debonding at the IPyC-SiC interface. The stress generated on both sides of this main crack causes SiC to experience tensile stress greater, leading to the complete fracture of the outer three coatings at an earlier time compared to the scenario with only a residual pore in SiC. Therefore, in engineering applications, particular attention should be given to avoiding and limiting the size of cracks in the IPyC layer. The complete fracture occurs at 18.18×10^7 s, the earliest among all the studied scenarios.

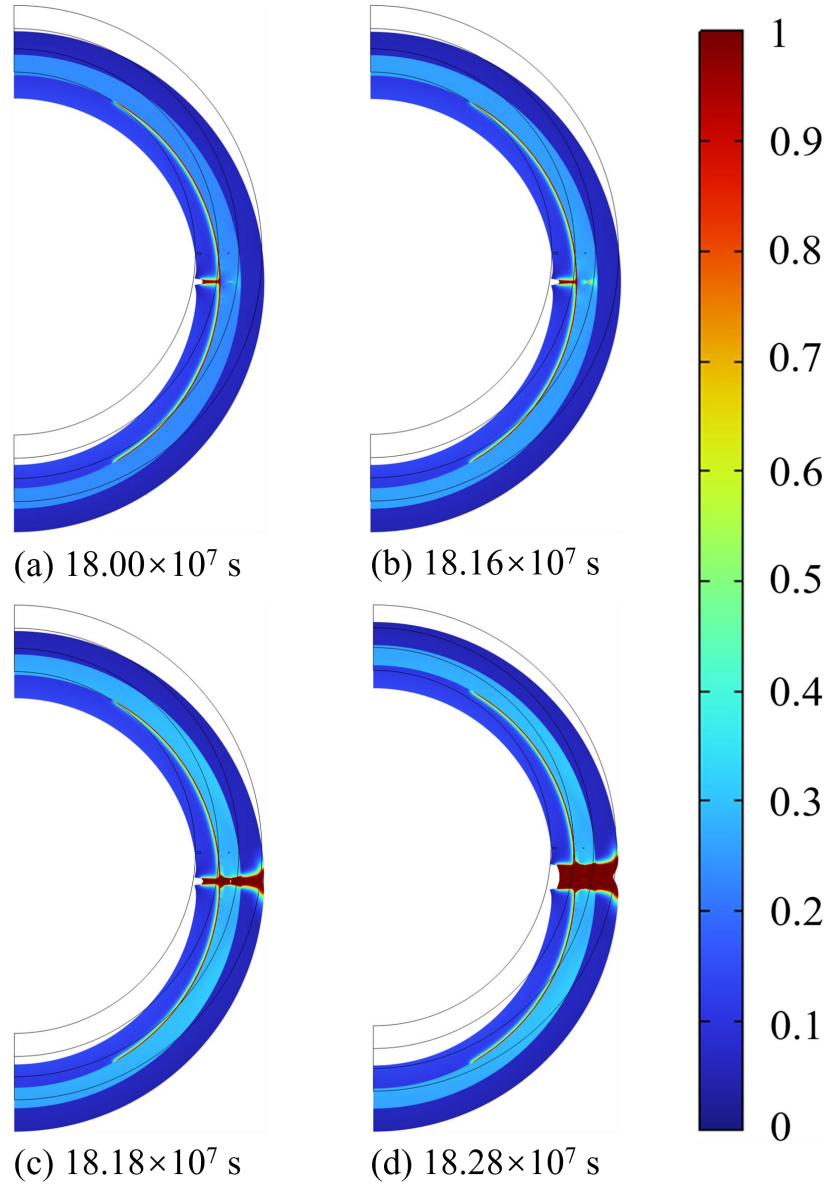


Fig. 27. Phase field when both a crack in the IPyC layer and a residual pore in the SiC layer coexist.

Overall, the presence of these defects provides geometric conditions for stress concentration, serving as the foundation for further crack propagation. However, in the early stages of burnup, crack propagation in the IPyC layer, primarily induced by irradiation, only leads to debonding between the IPyC and SiC layers rather than complete failure of the coating layers. The primary cause of complete fracture is the excessive internal gas pressure in the IPyC layer, which results from the high temperature and the accumulation of fission gas during the later stages of burnup due to prolonged operation. Therefore, before TRISO particles are deployed in space reactors, it is crucial to screen for particles with minimal defects and implement measures to maintain the structural integrity of the coating layers.

6. Conclusions

In this paper, a phase field model for analyzing the outer three coatings of

TRISO particles was developed using COMSOL Multiphysics. The fuel behavior was thoroughly considered, including material properties varying with condition parameters, burnup, irradiation effects, fission gas release, and gas pressure formation. To validate the accuracy of the model in simulating TRISO particle behavior, the model was compared with stress calculation results from other codes using the IAEA CRP-6 CASE 8 benchmark, and also validated with deformation and stress results from the typical BISON code for a complete TRISO particle. The comparison clearly demonstrated the accuracy of the TRISO particle simulation [20]. In addition, to validate the phase field model, it was applied to simulate a notched tensile plate and the Kalthoff experiment problem. The results confirmed that the phase field model constructed in this study could reliably simulate crack propagation characteristics in brittle fracture problems.

After that, this study analyzed the effects of common defects in TRISO particles, including pre-existing crack on the inner side of the IPyC layer, residual pores in the SiC layer, pre-existing crack on the outer side of the OPyC layer, and the combined presence of a crack in the IPyC layer and a residual pore in the SiC layer. The results show that, first, when a pre-crack deeper than 5.8 μm exists on the inner side of the IPyC layer, the crack will propagate outward toward the SiC layer. Upon reaching the interface, it deflects on both sides, causing debonding between the two layers. This crack propagation leads to higher tensile stress in the SiC layer near the crack tip, but it is insufficient to cause crack formation or fracture. As the pre-crack depth increases, the crack begins to propagate earlier, and the separation of the two layers occurs more rapidly. Second, when a pore with a radius greater than 0.2 μm exists in the SiC layer, cracks will form at the end of the burnup and propagate inward and outward, eventually causing complete fracture of the outer coatings. Even for perfect materials without defects, the maximum gas pressure that the outer coatings can withstand is 139 MPa. Third, the presence of a pre-crack on the outer side of the OPyC layer has a small impact during the early and mid-burnup stages. However, at the end of the burnup, the crack causes concentrated tensile stress at two locations on the outer surface of the SiC layer, changing the crack propagation path and causing two cracks to propagate inward, leading to the complete fracture of the coatings. Fourth, when both a crack on the inner side of the IPyC layer and a residual pore in the SiC layer coexist, the complete fracture of the outer coatings occurs earlier than when only the residual pore exists in the SiC layer.

In conclusion, these defects create conditions for stress concentration and crack propagation. For TRISO particles, efforts should be made to avoid these defects before deployment. Before TRISO particles are manufactured into FCM fuels and used in reactors, if material detection techniques such as using X-ray radiographs [79], are available, cracks in the IPyC layer exceeding 5.8 μm in length should be avoided, and residual pore radii in the SiC layer should not exceed 0.2 μm . Cracks in the OPyC layer should also be minimized. Additionally, even for perfect coating materials without defects, they cannot withstand gas pressures exceeding 139 MPa, or the TRISO particles will collapse. Therefore, it is fundamentally necessary to either modify the structure of SiC to enhance its strength, replace SiC with stronger

materials, or implement measures to expel fission gases from TRISO particles. As for future work, methods like PF-CZM [78, 80-82] more aligned with engineering practices can be developed to analyze the debonding of the IPyC and SiC layers, as well as the separation between TRISO particles and the FCM pellet matrix. Additionally, methods such as topology optimization [83] and multi-objective optimization [84] can be employed to optimize and improve the fuel, thereby enhancing its performance. Last but not least, cracks in the pellet and even fuel rods need to be simulated to promote the eventual application of FCM fuel in space reactors.

Acknowledgements

This work is Funded by Natural Science Foundation of Chongqing, China, 2023NSCQ-BHX0243.

References

- [1] S. Nasiri, G.R. Ansarifard, Neutronic design and analysis of the accident-tolerant fuel (ATF) application to VVER-1000 nuclear reactor as well as evaluation of dynamic parameters, *Nucl. Eng. Des.* 432 (2025), 113814. <https://doi.org/10.1016/j.nucengdes.2024.113814>.
- [2] N. Doncel, L. Martínez, P. Aragón, et al., R&D in advanced technology fuels (ATFs) in Spain, *Nucl. Eng. Des.* 424 (2024), 113246. <https://doi.org/10.1016/j.nucengdes.2024.113246>.
- [3] M. H. d. Toit, A. Mphofu, N. Mashilangako, Neutronic and thermal-hydraulic coupling of FCM and helium annular fuel as accident-tolerant fuel, *Nucl. Eng. Des.* 428 (2024), 113522. <https://doi.org/10.1016/j.nucengdes.2024.113522>.
- [4] C. Griesbach, T. Gerczak, C. McKinney, et al., Irradiation-condition dependent mechanisms controlling buffer densification and fracture in TRISO nuclear fuel particles, *J. Nucl. Mater.* 605 (2025), 155565. <https://doi.org/10.1016/j.jnucmat.2024.155565>.
- [5] T. Mauseth, M. L. Dunzik-Gougar, S. Meher, et al., Determining the tensile strength of fuel surrogate TRISO-coated particle buffer, IPyC, and buffer-IPyC interlayer regions, *J. Nucl. Mater.* 583 (2023), 154540. <https://doi.org/10.1016/j.jnucmat.2023.154540>.
- [6] R.L. Seibert, T.J. Gerczak, G.W. Helmreich, et al., AGR-2 irradiated TRISO particle IPyC/SiC interface analysis using FIB-SEM tomography, *J. Nucl. Mater.* 573 (2023), 154104. <https://doi.org/10.1016/j.jnucmat.2022.154104>.
- [7] R. L. Seibert, B. C. Jolly, M. Balooch, et al., Production and characterization of TRISO fuel particles with multilayered SiC, *J. Nucl. Mater.* 515 (2019) 215-226. <https://doi.org/10.1016/j.jnucmat.2018.12.024>.
- [8] M. MW. Silicon Carbide Integrity in Triso Fuel Particles. Order No. 30714552 ed. University of Pretoria (South Africa); 2015.

<https://www.proquest.com/dissertations-theses/silicon-carbide-integrity-triso-fuel-particles/docview/2901811218/se-2>.

[9] Q. Zeng, Z. He, X. Pan, et al., Effect of Coating Temperature on Microstructure and Properties of the SiC Layer in TRISO-Coated Particles, *J. Nucl. Mater.* 3 (2023). https://doi.org/10.1007/978-981-19-8899-8_28.

[10] A. Bratten, V. Jalan, M. Shi, et al., High-temperature oxidation behavior of the SiC layer of TRISO particles in low-pressure oxygen, *J. Am. Ceram. Soc.* 106(6) (2023) 3922-3933. <https://doi.org/10.1111/jace.19032>.

[11] N. Baghdasaryan, T. Kozlowski, Review of Progress in Coated Fuel Particle Performance Analysis, *Nucl. Sci. Eng.* 194(3) (2019) 169–180. <https://doi.org/10.1080/00295639.2019.1686882>.

[12] P. A. Demkowicz, B. Liu, H. D. Hunn, Coated particle fuel: Historical perspectives and current progress, *J. Nucl. Mater.* 515 (2019) 434-450. <https://doi.org/10.1016/j.jnucmat.2018.09.044>.

[13] G. R. Bower, S. A. Ploger, P. A. Demkowicz, et al., Measurement of kernel swelling and buffer densification in irradiated UCO-TRISO particles, *J. Nucl. Mater.* 486 (2017) 339-349. <https://doi.org/10.1016/j.jnucmat.2017.01.006>.

[14] J.D. Hales, R.L. Williamson, S.R. Novascone, et al., Multidimensional multiphysics simulation of TRISO particle fuel, *J. Nucl. Mater.* 443(1-3) (2013) 531-543. <https://doi.org/10.1016/j.jnucmat.2013.07.070>.

[15] C. Zhang, Y. Wu, S. Liu, et al., Multidimensional multiphysics modeling of TRISO particle fuel with SiC/ZrC coating using modified fission gas release model, *Ann. Nucl. Energy.* 145 (2020), 107599. <https://doi.org/10.1016/j.anucene.2020.107599>.

[16] C. Zhang, Y. Wu, Y. He, et al., Investigation on thermo-mechanical performance of fully ceramic microencapsulated fuel, *J. Nucl. Mater.* 556 (2021), 153171. <https://doi.org/10.1016/j.jnucmat.2021.153171>.

[17] S. Tang, L. Zhu, Q. Lian, et al., Design and optimization of three segmented thermoelectric generator for nuclear reactor application, *Prog. Nucl. Energy.* 173 (2024), 105243. <https://doi.org/10.1016/j.pnucene.2024.105243>.

[18] Y. Wu, S. Tang, L. Zhu, et al., Transient analysis of megawatt-level space gas-cooled reactor coupled with He-Xe Brayton cycle system, *Appl. Therm. Eng.* 260 (2025), 124962. <https://doi.org/10.1016/j.applthermaleng.2024.124962>.

[19] S. Tang, Q. Lian, L. Zhu, et al., Thermal-electrical coupling analysis of the static heat pipe cooled reactor under heat pipe failure condition, *Nucl. Eng. Des.* 417 (2024), 112812. <https://doi.org/10.1016/j.nucengdes.2023.112812>.

[20] L. Peng, Y. Yang, S. Li, et al., Investigation on irradiated-thermal-mechanical coupling performance and failure behaviors of TRISO particle fuel for space reactor applications, *Prog. Nucl. Energy.* 180 (2025), 105633. <https://doi.org/10.1016/j.pnucene.2025.105633>.

[21] D. A. Petti, J. T. Maki, J. Buongiorno, et al., Key Differences in the Fabrication, Irradiation and Safety Testing of U.S. and German TRISO-coated Particle Fuel and Their Implications on Fuel Performance, 2002. INEEL/EXT-02-00300. <https://digital.library.unt.edu/ark:/67531/metadc888178/>.

- [22] Y. Zhong, H. S. Lai, J. Guo, P. Du, et al., Small punch test for investigating circumferential creep in cladding tubes, *Int. J. Mech. Sci.* 267 (2024), 109001. <https://doi.org/10.1016/j.ijmecsci.2024.109001>.
- [23] Y. Zhao, X. Gong, S. Ding, et al., A numerical method for simulating the non-homogeneous irradiation effects in full-sized dispersion nuclear fuel plates, *Int. J. Mech. Sci.* 81 (2014) 174-183. <https://doi.org/10.1016/j.ijmecsci.2014.02.012>.
- [24] M. Klinsmann, D. Rosato, M. Kamlah, et al., An assessment of the phase field formulation for crack growth, *Comput. Methods Appl. Mech. Eng.* 294 (2015) 313-330. <https://doi.org/10.1016/j.cma.2015.06.009>.
- [25] A. R. Ingraffea, V. Saouma, Numerical modeling of discrete crack propagation in reinforced and plain concrete, *Fract. Mech. Concr.: Struct. Appl. Numer. Calc.* 4 (1985) 171-225. https://doi.org/10.1007/978-94-009-6152-4_4.
- [26] N. Moës, T. Belytschko, Extended finite element method for cohesive crack growth, *Eng. Fract. Mech.* 69(7) (2002) 813-833. [https://doi.org/10.1016/S0013-7944\(01\)00128-X](https://doi.org/10.1016/S0013-7944(01)00128-X).
- [27] L. Chen, T. Rabczuk, S.P.A. Bordas, et al., Extended finite element method with edge-based strain smoothing (ESm-XFEM) for linear elastic crack growth, *Comput. Methods Appl. Mech. Eng.* 209-212 (2012) 250-265. <https://doi.org/10.1016/j.cma.2011.08.013>.
- [28] N.A. Collins-Craft, F. Bourrier, V. Acary, On the formulation and implementation of extrinsic cohesive zone models with contact, *Comput. Methods Appl. Mech. Eng.* 400 (2022), 115545. <https://doi.org/10.1016/j.cma.2022.115545>.
- [29] Z. Song, B. Han, J. Zhang, et al., Numerical analysis of mesoscale fatigue cracking behavior in concrete based on cohesive zone model, *Struct.* 70 (2024), 107777. <https://doi.org/10.1016/j.istruc.2024.107777>.
- [30] T. Metzler, E. Gaganidze, J. Aktaa, Prediction of fracture toughness of a reactor pressure vessel steel in the ductile-to-brittle transition region based on a probabilistic cohesive zone model approach, *J. Nucl. Mater.* 605 (2025), 155556. <https://doi.org/10.1016/j.jnucmat.2024.155556>.
- [31] Z. Shirzadeh, M. Fakoore, Z. Daneshjoo, Simulating delamination in composite laminates with fracture process zone effects: A novel cohesive zone modeling approach, *Eng. Fract. Mech.* 315 (2025), 110834. <https://doi.org/10.1016/j.engfracmech.2025.110834>.
- [32] Thanh Chau-Dinh, Goangseup Zi, Phill-Seung Lee, et al., Phantom-node method for shell models with arbitrary cracks, *Comput. Struct.* 92-93 (2012) 242-256. <https://doi.org/10.1016/j.compstruc.2011.10.021>.
- [33] L. Yang, F. Vasilina, H. Nan, et al., A regularized phenomenological multiscale damage model, *Int. J. Numer. Methods Eng.* 99(12) (2014) 867-887. <https://doi.org/10.1002/nme.4705>.
- [34] Z. Tian, A. Jiang, Modeling the Propagation of a Prefabricated Brittle Crack Using Phase-field Method within the Framework of ABAQUS, *KSCE J. Civ. Eng.* 28(7) (2024) 3042-3053. <https://doi.org/10.1007/s12205-024-1944-0>.
- [35] P.C. Sidharth, B.N. Rao, An open-source moose implementation of phase-field modeling of fracture in functionally graded materials, *Procedia Struct.*

Integrity. 58 (2024) 115-121. <https://doi.org/10.1016/j.prostr.2024.05.019>.

[36] Hirshikesh, D. Schneider, B. Nestler, Realization of adaptive mesh refinement for phase-field model of thermal fracture within the FEniCS framework, Eng. Fract. Mech. 293 (2023), 109676. <https://doi.org/10.1016/j.engfracmech.2023.109676>.

[37] Y. Wang, X. Hou, Y. Wang, Thermo-gaseous-mechanical coupling phase-field model for brittle crack propagation in tungsten, J. Mater. Res. Technol. 33 (2024) 7418-7433. <https://doi.org/10.1016/j.jmrt.2024.11.145>.

[38] Sana Shahoveisi, Mohammad Vahab, Babak Shahbodagh, et al., Phase-field modelling of dynamic hydraulic fracturing in porous media using a strain-based crack width formulation, Comput. Methods Appl. Mech. Eng. 429 (2024), 117113. <https://doi.org/10.1016/j.cma.2024.117113>.

[39] S. Zhou, T. Rabczuk, X. Zhuang, Phase field modeling of quasi-static and dynamic crack propagation: COMSOL implementation and case studies, Adv. Eng. Softw. 122 (2018) 31-49. <https://doi.org/10.1016/j.advengsoft.2018.03.012>.

[40] Y. Zhang, J. Sun, C. Liu, et al., Phase field modeling of coupling evolution of fracture and dielectric breakdown in ferroelectric materials, Int. J. Mech. Sci. 236 (2022), 107747. <https://doi.org/10.1016/j.ijmecsci.2022.107747>.

[41] X. Wu, M. Chen, L. Ke, An electro-thermo-mechanical coupling phase-field model of defect evolution induced by electromigration in interconnects, Int. J. Mech. Sci. 285 (2025), 109792. <https://doi.org/10.1016/j.ijmecsci.2024.109792>.

[42] W. Tang, S. Wen, H. Hou, et al., Phase-field simulation and machine learning of low-field magneto-elastocaloric effect in a multiferroic composite, Int. J. Mech. Sci. 275 (2024), 109316. <https://doi.org/10.1016/j.ijmecsci.2024.109316>.

[43] D. Yi, Z. Yang, L. Yi, J. Liu, et al., Phase-field model of hydraulic fracturing in thermoelastic-plastic media, Int. J. Mech. Sci. 283 (2024), 109750. <https://doi.org/10.1016/j.ijmecsci.2024.109750>.

[44] J. Luo, Q. Wang, W. Zhou, et al, A coupled phase-field model for sulfate-induced concrete cracking, Int. J. Mech. Sci. 283 (2024), 109694. <https://doi.org/10.1016/j.ijmecsci.2024.109694>.

[45] J. Liu, Z. Yang, L. Yi, et al., Cohesive phase-field model for dynamic fractures in coal seams, Int. J. Mech. Sci. 282 (2024), 109617. <https://doi.org/10.1016/j.ijmecsci.2024.109617>.

[46] J. Zhao, Y. Frank Cheng, A phase field method for predicting hydrogen-induced cracking on pipelines, Int. J. Mech. Sci. 283 (2024), 109651. <https://doi.org/10.1016/j.ijmecsci.2024.109651>.

[47] H. Zhang, E. López-Honorato, A. Javed, et al., A Study of the Microstructure and Vickers Indentation Fracture Toughness of Silicon Carbide Coatings on TRISO Fuel Particles, J. Am. Ceram. Soc. 95(3) (2012) 1086-1092. <https://doi.org/10.1111/j.1551-2916.2011.05044.x>.

[48] K. I. Montoya, E. G. Herbert, D. P. Schappel, et al., Micromechanical response of SiC-OPyC layers in TRISO fuel particles, J. Nucl. Mater. 606 (2025), 155654. <https://doi.org/10.1016/j.jnucmat.2025.155654>.

[49] F. Cao, W. Hao, F. Guo, et al., Effects of water vapor on the oxidation and

the fracture strength of SiC layer in TRISO fuel particles, J. Am. Ceram. Soc. 100(5) 2154-2165. <https://doi.org/10.1111/jace.14723>.

[50] H. M. Lee, K. Park, J. Park, et al., High-Temperature Fracture Strength of a CVD-SiC Coating Layer for TRISO Nuclear Fuel Particles by a Micro-Tensile Test, J. Korean Ceram. Soc. 52 (2015) 441-448. <https://doi.org/10.4191/kcers.2015.52.6.441>.

[51] A. M. Recuero, G. Singh, W. Jiang, Fracture mechanics approach to TRISO fuel particle failure analysis, J. Nucl. Mater. 596 (2024), 155083. <https://doi.org/10.1016/j.jnucmat.2024.155083>.

[52] Y. Li, Q. Wei, L. Li, Analysis of micro-defect-induced cracking in the IPyC layer of TRISO particle with the XFEM, Eng. Comput. 41 (2024) 1973-1986. <https://doi.org/10.1108/EC-11-2023-0873>.

[53] J. Tan, Y. Wu, Q. Li, et al., Phase field modeling of irradiation-induced shrinkage fracture in TRISO fuel particle, J. Nucl. Mater. 592 (2024), 154963. <https://doi.org/10.1016/j.jnucmat.2024.154963>.

[54] G.K. Miller, D.A. Petti, J.T. Maki, et al., PARFUME Theory and Model Basis Report, Idaho National Laboratory, 2009. INL/EXT-08-14497. <https://doi.org/10.2172/968587>.

[55] D. P. Schappel, Improvements to the Predictive Capability of FCM Fuel Performance Modeling, PhD diss., University of Tennessee, 2017. https://trace.tennessee.edu/utk_graddiss/4646.

[56] L. L. Snead, T. Nozawa, Y. Katoh, et al., Handbook of SiC properties for fuel performance modeling, J. Nucl. Mater. 371(1-3) (2007) 329-377. <https://doi.org/10.1016/j.jnucmat.2007.05.016>.

[57] D. R. Olander, Fundamental aspects of nuclear reactor fuel elements: solutions to problems, Technical information center, Energy research and development administration, 1976. <https://doi.org/10.2172/7290222>.

[58] J. D. Hales, R. L. Williamson, S. R. Novascone, et al., BISON Theory Manual The Equations Behind Nuclear Fuel Analysis, Idaho National Laboratory, Fuel Modeling and Simulation Department, INL/EXT-13-29930 Rev. 3, 2016. <https://doi.org/10.2172/1374503>.

[59] D. Petti, P. Martin, M. Philip, R. Ballinger, Development of improved models and designs for coated-particle gas reactor fuels. Technical Report, INL/EXT-05-02615, December 2004. <https://doi.org/10.2172/911237>.

[60] A.H. Booth, A method of calculating fission gas diffusion from UO₂ fuel and its application to the x-2-f loop test, Atomic Energy of Canada. AECL-496, September 1957. <https://www.osti.gov/servlets/purl/4331839>.

[61] T. Kogai, Modelling of fission gas release and gaseous swelling of light water reactor fuels, J. Nucl. Mater. 244(2) (1997) 131-140. [https://doi.org/10.1016/S0022-3115\(96\)00731-3](https://doi.org/10.1016/S0022-3115(96)00731-3)

[62] K. Forsberg, A.R. Massih, Diffusion theory of fission gas migration in irradiated nuclear fuel UO₂, J. Nucl. Mater. 135(2-3) (1985) 140-148. [https://doi.org/10.1016/0022-3115\(85\)90071-6](https://doi.org/10.1016/0022-3115(85)90071-6).

[63] Y. Cui, Y. Huo, S. Ding, et al., An analytical solution for simulation of the fission gas behaviors with time-dependent piece-wise boundary resolution, J. Nucl.

Mater. 424(1-3) (2012) 109-115. <https://doi.org/10.1016/j.jnucmat.2012.02.010>.

[64] A. A. Griffith. The Phenomena of Rupture and Flow in Solids, Ser. A, Math. Phys. 221 (1921) 163-198. <https://www.jstor.org/stable/91192>.

[65] C. Miehe, M. Hofacker, F. Welschinger, A phase field model for rate-independent crack propagation: Robust algorithmic implementation based on operator splits, Comput. Methods Appl. Mech. Eng. 199(45-48) (2010) 2765-2778. <https://doi.org/10.1016/j.cma.2010.04.011>.

[66] M. J. Borden, C. V. Verhoosel, M. A. Scott, et al., A phase-field description of dynamic brittle fracture, Comput. Methods Appl. Mech. Eng. 217-220 (2012) 77-95. <https://doi.org/10.1016/j.cma.2012.01.008>.

[67] C. Miehe, F. Welschinger, M. Hofacker, Thermodynamically consistent phase-field models of fracture: Variational principles and multi-field FE implementations. Int. J. Numer. Meth. Eng. 83 (2010) 1273-1311. <https://doi.org/10.1002/nme.2861>.

[68] K. Bongartz, E. Gyarmati, H. Schuster, K. Täuber, The Brittle Ring Test: A method for measuring strength and young's modulus on coatings of HTR fuel particles, J. Nucl. Mater. 62(2-3) (1976) 123-137. [https://doi.org/10.1016/0022-3115\(76\)90012-X](https://doi.org/10.1016/0022-3115(76)90012-X).

[69] INTERNATIONAL ATOMIC ENERGY AGENCY, Advances in High Temperature Gas Cooled Reactor Fuel Technology, Technical Report IAEA-TECDOC-1674, 2013. <https://www.iaea.org/publications/10451/advances-in-high-temperature-gas-cooled-reactor-fuel-technology>

[70] J.F. Kalthoff, Modes of dynamic shear failure in solids, Int. J. Fract. 101 (2000) 1-31. <https://doi.org/10.1023/A:1007647800529>.

[71] S. Liu, G. Fang, J. Liang, et al., A coupling model of XFEM/peridynamics for 2D dynamic crack propagation and branching problems, Theor. Appl. Fract. Mech. 108 (2020), 102573. <https://doi.org/10.1016/j.tafmec.2020.102573>.

[72] J. Song, P. M. A. Areias, T. Belytschko. A method for dynamic crack and shear band propagation with phantom nodes, Int. J. Numer. Meth. Eng. 67 (2006) 868-893. <https://doi.org/10.1002/nme.1652>.

[73] Z. M. Krajewska, T. Buchwald, A. Drożdżiel, Mechanical defects in the “p-TRISO”-particle covering layers obtained through the ion implantation process, Ann. Nucl. Energy. 190 (2023), 109897. <https://doi.org/10.1016/j.anucene.2023.109897>.

[74] S. Liu, Y. Li, P. Chen, et al., Effect of residual pore structure on the performance of TRISO particle fuel, Front. Mater. 9 (2022), 1072255. <https://doi.org/10.3389/fmats.2022.1072255>.

[75] A. Baux, S. Jacques, A. Allemand, et al., Complex geometry macroporous SiC ceramics obtained by 3D-printing, polymer impregnation and pyrolysis (PIP) and chemical vapor deposition (CVD), J. Eur. Ceram. Soc. 41(6) (2021) 3274-3284. <https://doi.org/10.1016/j.jeurceramsoc.2021.01.008>.

[76] T.A. Haynes, A. Battistini, A.J. Leide, et al., Peridynamic modelling of cracking in TRISO particles for high temperature reactors, J. Nucl. Mater. 576 (2023),

154283. <https://doi.org/10.1016/j.jnucmat.2023.154283>.

[77] J. T. Maki, D. A. Petti, D. L. Knudson, et al., The challenges associated with high burnup, high temperature and accelerated irradiation for TRISO-coated particle fuel, *J. Nucl. Mater.* 371(1-3) (2007) 270-280. <https://doi.org/10.1016/j.jnucmat.2007.05.019>.

[78] V. Carollo, J. Reinoso, M. Paggi, Modeling complex crack paths in ceramic laminates: A novel variational framework combining the phase field method of fracture and the cohesive zone model, *J. Eur. Ceram. Soc.* 38(8) (2018) 2994-3003. <https://doi.org/10.1016/j.jeurceramsoc.2018.01.035>.

[79] M. Stringer, C.V. Anghel, B.M. van der Ende, Identification of TRISO pebbles at arbitrary orientation using pairs of X-ray radiographs, *Nucl. Instrum. Methods Phys. Res., Sect. A.* 1066 (2024), 169613. <https://doi.org/10.1016/j.nima.2024.169613>.

[80] Dusane, A. R. Budarapu, P. R. Pradhan, et al., Simulation of bridging mechanisms in complex laminates using a hybrid PF-CZM method, *Mech. Adv. Mater. Struct.* 29(28) (2022) 7743–7771. <https://doi.org/10.1080/15376494.2021.2006835>.

[81] C. Zou, H. Yang, G. Chen, et al., Internal-interfacial cracking interaction: Combined phase-field and discontinuous Galerkin/cohesive zone modeling, *Int. J. Mech. Sci.* 273 (2024), 109211. <https://doi.org/10.1016/j.ijmecsci.2024.109211>.

[82] Liu, Y. Wang, W. Wu, A modified phase-field model for cohesive interface failure in quasi-brittle solids, *Int. J. Mech. Sci.* 252 (2023), 108368. <https://doi.org/10.1016/j.ijmecsci.2023.108368>.

[83] Z. Huang, C. Liu, Q. Sun, Dynamics analysis and multi-objective optimization for a dry friction damper, *Int. J. Mech. Sci.* 287 (2025), 109930. <https://doi.org/10.1016/j.ijmecsci.2025.109930>.

[84] Y. Liu, Y. Oda, K. Sasahara, Shape and topology optimization method with generalized topological derivatives, *Int. J. Mech. Sci.* 284 (2024), 109735. <https://doi.org/10.1016/j.ijmecsci.2024.109735>.